The evolution of cluster E and S0 galaxies measured from the Fundamental Plane*

Inger Jørgensen[1,2 †‡§] Marijn Franx[3,4,5 ‡§], Jens Hjorth[6,7,8 §], Pieter G. van Dokkum[3,5 §]

[1]*McDonald Observatory, The University of Texas at Austin, RLM 15.308, Austin, TX 78712, USA*
[2]*Gemini Observatory, 670 N. A'ohoku Pl., Hilo, HI 96720, USA (Postal address for IJ)*
[3]*Kapteyn Institute, P.O.Box 800, 9700 AV Groningen, The Netherlands*
[4]*Center for Astrophysics, 60 Garden Street, Cambridge, MA 02138, USA*
[5]*Leiden Observatory, P.O.Box 9513, 2300 RA Leiden, The Netherlands (Postal address for MF and PvD)*
[6]*Institute of Astronomy, Madingley Road, Cambridge CB3 0HA, UK*
[7]*NORDITA, Blegdamsvej 17, DK-2100 Copenhagen Ø, Denmark*
[8]*Astronomical Observatory, University of Copenhagen, Juliane Maries Vej 30, DK-2100 Copenhagen Ø, Denmark (Postal address for JH)*

May 5, 1999, accepted for publication in Mon. Not. Royal Astron. Sco., Gemini Preprint #43

ABSTRACT

Photometry has been obtained for magnitude limited samples of galaxies in the two rich clusters Abell 665 (37 galaxies) and Abell 2218 (61 galaxies). Both clusters have a redshift of 0.18. The limiting magnitude of the samples is 19^{m} in the I-band. Spectroscopy has been obtained for seven galaxies in A665 and nine galaxies in A2218, all of which also have available photometry. Spectroscopy has been obtained for two additional galaxies in A2218, one of which is a background galaxy.

Effective radii r_{e} and mean surface brightnesses $<I>_{\mathrm{e}}$ were derived from the photometry. The typical uncertainties are ± 0.078 in $\log r_{\mathrm{e}}$ and ± 0.12 in $\log <I>_{\mathrm{e}}$. The combination $\log r_{\mathrm{e}} + 0.82 \log <I>_{\mathrm{e}}$ that enters the Fundamental Plane (FP) has an uncertainty of only ± 0.018. The spectroscopy was used for measurements of the velocity dispersions, σ. The typical uncertainty is ± 0.023 on $\log \sigma$.

The data are used to establish the FP, $\log r_{\mathrm{e}} = \alpha \log \sigma + \beta \log <I>_{\mathrm{e}} + \gamma$, for the clusters. The FP for these two clusters adds important knowledge about the properties of E and S0 galaxies in the relatively unexplored redshift interval 0.05 to 0.3. We have compared the FP for A665 and A2218 with the FP for the three clusters CL0024+16, CL1358+62 and MS2053-04 with redshifts between 0.33 and 0.58, and with the FP for the Coma cluster. The scatter around the FP is similar for all six clusters. We find that the FP for the intermediate redshift clusters has a smaller coefficient α than found for the Coma cluster and other nearby clusters. This may either be caused by selection effects for the intermediate redshift clusters or by differences in the evolution of low luminosity galaxies and high luminosity galaxies.

The mass-to-light (M/L) ratios, as measured from the FP, change with redshift. At z=0.18 the M/L ratio for photometry in Gunn r in the rest frame of the clusters is (11 ± 7)% smaller than for the Coma cluster. Using the data for A665 and A2218 together with the previously published data for CL0024+16, CL1358+62 and MS2053-04, we find that the M/L ratios for photometry calibrated to Gunn r change with redshift as $\Delta \log M/L_r = (-0.26 \pm 0.06)\Delta z$ for $q_{\mathrm{o}} = 0.5$. This change in the M/L ratio is equivalent to the absolute magnitudes changing as $\Delta M_{r_{\mathrm{T}}} = (-0.65 \pm 0.15)\Delta z$. These new results are consistent with the previously published analysis for CL0024+16, CL1358+62 and MS2053-04.

For $q_{\mathrm{o}} = 0.5$ the results are consistent with passive evolution of a stellar population which formed at a redshift larger than five. For $q_{\mathrm{o}} = 0.15$ the formation redshift must be larger than 1.7. Our new data for A665 and A2218 confirm the gradual and slow evolution of the bright E and S0 galaxies. However, possible star formation in E and S0 galaxies during the last 3-4 Gyr of the history of the Universe, as well as the selection effects complicate the interpretation of the data.

Key words: galaxies: clusters: individual: Abell 665, Abell 2218 – galaxies: elliptical and lenticular, cD – galaxies: evolution – galaxies: stellar content.

1 INTRODUCTION

Observational studies show that the formation and evolution of galaxies is a complex process, which may involve interactions, star bursts and infall (e.g., Dressler et al. 1994ab; Lilly et al. 1996; Moore et al. 1996). It has also been found that some nearby E and S0 galaxies may have experienced star formation in the last 3-4 Gyr. Caldwell et al. (1993) found some E and S0 galaxies in the Coma cluster to have post-starburst spectra, and Faber et al. (1995) suggest that nearby field E galaxies have a substantial variation in the mean age of their stellar populations.

In order to study the evolution of galaxies we need to study both the morphological evolution as well as the evolution of the luminosities and the mass-to-light (M/L) ratios of the galaxies. High-resolution imaging with the *Hubble Space Telescope* (HST) and from the ground, combined with spectroscopy from the ground make it possible to carry out this kind of studies. Studies of the morphological evolution show that the fraction of spiral galaxies and irregular galaxies in clusters was higher at larger redshifts (e.g., Dressler et al. 1994ab; Oemler et al. 1997; Dressler et al. 1997; Couch et al. 1998). A detailed investigation of how the luminosities of disk galaxies change with redshift is possible using the Tully-Fisher (1977) relation. Vogt et al. (1996) established the Tully-Fisher relation for a sample of field galaxies with redshifts between 0.1 and 1 and found a luminosity evolution in the B-band of $\approx 0\overset{\mathrm{m}}{.}6$ between $z = 1$ and the present.

The Fundamental Plane (FP) (Dressler et al. 1987; Djorgovski & Davis 1987) for elliptical galaxies makes it possible to study how the luminosities and the M/L ratios of these galaxies change with redshift. Also, S0 galaxies in nearby clusters follow the FP (e.g., Jørgensen, Franx & Kjærgaard 1996, hereafter JFK96). The FP relates the effective radius, $r_{\rm e}$, the mean surface brightness within this radius, $<I>_{\rm e}$, and the (central) velocity dispersion, σ, in a tight relation, which is linear in log-space. For 226 E and S0 galaxies in nearby clusters JFK96 found $\log r_{\rm e} = 1.24 \log \sigma - 0.82 \log <I>_{\rm e} + {\rm cst}$, for photometry in Gunn r. This relation may be interpreted as $M/L \propto M^{0.24} {r_{\rm e}}^{-0.02}$ (cf., Faber et al. 1987). The change of the M/L ratio with the mass is partly caused by changes in the stellar populations. Some of the apparent change may also be explained by non-homology of the galaxies (e.g., Hjorth & Madsen 1995). Throughout this paper we assume that the FP implies a relation between the M/L ratios and the masses of the galaxies.

The scatter of the FP is very low, equivalent to a scatter of 23% in the M/L ratio (e.g., JFK96). Thus, the FP offers the possibility of detecting even small differences in the M/L ratios by observing a handful of galaxies in a distant cluster.

The FP has been used to study the evolution of the M/L ratios of cluster galaxies as a function of redshift up to a redshift of 0.83 (van Dokkum & Franx 1996; Kelson et al. 1997; Bender et al. 1998; van Dokkum et al. 1998; Pahre, Djorgovski & de Carvalho 1999). All of these studies find the M/L ratios of the galaxies to increase slowly with decreasing redshift. Only the study by Pahre et al. contains clusters with redshifts between 0.05 and 0.3. In this paper we establish the FP for the two rich clusters Abell 665 and Abell 2218. Both clusters have a redshift of 0.18, adding data to a redshift interval not well-covered by the previous studies.

We use the data for A665 and A2218, data for the three clusters studied by van Dokkum & Franx (1996) and Kelson et al. (1997), and data for the Coma and the HydraI clusters to study how the FP and the M/L ratios of the E and S0 galaxies change with redshift. The full sample covers about half the age of the Universe.

The available photometry and spectroscopy, as well as the derivation of the photometric and spectroscopic parameters is described in Sections 2 and 3, respectively. The details of the data reduction are provided in Appendix A and B. Appendix A also contains photometric parameters (effective radii, mean surface brightnesses and colors) of magnitude limited samples of galaxies in A665 and A2218. Section 4 briefly describes the data for the other clusters. The FP is analyzed in Section 5. In this section we also discuss the evolution of the M/L ratios of the galaxies. The conclusions are summarized in Section 6.

2 THE PHOTOMETRY

The central parts of the two rich clusters Abell 665 and Abell 2218 were observed with the Nordic Optical Telescope (NOT), La Palma, in March 1994. Observations were done in the I-band and the V-band. The sizes of the observed fields are $3\overset{\prime}{.}4 \times 2\overset{\prime}{.}7$ for A665 and $2\overset{\prime}{.}8 \times 3\overset{\prime}{.}5$ for A2218. Table 1 summarizes the instrumentation for the observations. The I-band images were taken as individual 600 sec exposures, with a few shorter exposures. The total exposure time, the seeing and the sky brightness of each of the final co-added images are given in Table 2. The V-band images were taken on another night than the I-band images, and have rather poor seeing.

A665 was observed with the HST with the Wide-Field-Planetary-Camera 2 (WFPC2) in the filters F606W and F814W. Two fields were observed giving a total coverage of approximately 9.4 square arc-minutes on the WF chips. For A2218 we use HST/WFPC2 archival data obtained in the F702W filter. One field in Abell 2218 was observed with the HST, covering approximately 4.7 square arc-minutes on the WF chips. The images were taken as individual exposures with exposure times between 1600 sec and 2300 sec. The total exposure times for the co-added images are given in Table 3.

⋆ Based in part on observations made with the NASA/ESA *Hubble Space Telescope* obtained at the Space Telescope Science Institute, which is operated by AURA under NASA contract NAS5-26555; the Multiple Mirror Telescope, a joint facility of the Smithsonian Institution and the University of Arizona; and the Nordic Optical Telescope, operated on the island of La Palma jointly by Denmark, Finland, Iceland, Norway and Sweden, in the Spanish Observatorio del Roque de los Muchachos of the Instituto de Astrofisica de Canarias.

† Hubble Fellow

‡ Visiting Astronomer, Kitt Peak Observatory, a division of National Optical Astronomy Observatories, which is operated by AURA under contract with the National Science Foundation.

§ E-mail: ijorgensen@gemini.edu, franx@strw.leidenuniv.nl, jens@astro.ku.dk, dokkum@strw.leidenuniv.nl

Table 1. Instrumentation

	Photometry		Spectroscopy	
Dates	March 4-9, 1994	Sept.-Dec., 1994	Jan. 18-19, 1991	June 6-8, 1994
Telescope	NOT, LaPalma	HST	MMT	KPNO 4m
Camera/Spec.	Astromed	WFPC2	Red Channel Spec.	R&C Spec.
CCD	EEV 1152×770	Loral	TI5	T2KB
r.o.n.	4.5 e^-	5.0 e^-	9.0 e^-	7.4 e^-
gain	0.9 e^-/ADU	7.5 e^-/ADU	2.0 e^-/ADU	2.6 e^-/ADU
Pixel scale	0.1635″/pixel	0.0996″/pixel^a	0.6″/pixel	0.69″/pixel
Slit width	...	...	1.8″	1.9″
Spectral res., σ	...	...	1.71Å	1.38Å
Wavelength range	...	...	5780-6420Å	4255-6970Å^b
Cluster(s)	A665, A2218	A665, A2218	A665	A2218

Notes. ^{a} All galaxies studied in this paper are imaged on the WF chips of WFPC2. ^{b} The unvignetted range is 4550-6500Å.

Table 2. NOT images

Image	Filter	$t_{\rm exp}$ [sec]	seeing [″]	$m_{\rm sky}$ [$^{\rm m}$/arcsec^2]
A665 field 1	I	9600	0.66	20.0
A665 field 1	V	1200	1.86	21.8
A665 field 2	I	5874	0.60	19.6
A665 field 2	V	1200	2.03	21.8
A2218 field 1	I	5400	0.70	19.3
A2218 field 1	V	1200	3.33	21.2
A2218 field 2	I	5400	0.82	19.4
A2218 field 2	V	1200	4.23	21.2

Notes. The seeing is measured as the full-width-half-maximum (FWHM) of a Gaussian fit to the core of images of stars. A665 field 1 is centered 0.′6 east and 0.′3 south of the BCG; field 2 is offset 1.′7 to the west of field 1. A2218 field 1 is centered 0.′3 to the south of the BCG; field 2 is offset 1.′7 to the north of field 1.

Table 3. HST images

Image	Filter	$t_{\rm exp}$ [sec]
A665 field 1	F606W	4400
A665 field 1	F814W	4400
A665 field 2	F606W	5100
A665 field 2	F814W	4800
A2218	F702W	6500

Notes. A665 field 1 is centered 0.′3 south-east of the BCG. A665 field 2 is centered 1.′7 west of the BCG. The observation of A2218 is centered 0.′9 east of the BCG.

The basic reductions of the images are described in Appendix A, which also covers the calibration of the photometry to the standard passbands I_c and V. In the following we describe the determination of the global photometric parameters (effective radii and mean surface brightnesses) and the calibration of the photometry to Gunn r and Johnson V in the rest frames of the clusters.

2.1 Global parameters

Determination of the effective radius, $r_{\rm e}$, and the mean surface brightness inside this radius, $<\mu>_{\rm e}$, was done following the technique described by van Dokkum & Franx (1996). This technique uses the full 2-dimensional information in the image. Each galaxy is fit with a 2-dimensional model, taking the point-spread-function (PSF) into account. The output from the fit is the center of the galaxy (x,y), the effective radius, $r_{\rm e}$, the surface brightness at the effective radius, $I_{\rm e}$, the ellipticity, ϵ, the position angle of the major axis and the level of the sky background. All galaxies presented here were fitted with $r^{1/4}$ profiles. The mean surface brightness $<\mu>_{\rm e}$ was derived from the local surface brightness at $r_{\rm e}$ under the assumption that the galaxies have $r^{1/4}$ profiles.

The PSF images for the NOT I-band images were constructed from 2-3 well-exposed stars in each image. The PSF images have a size of 10.″5×10.″5. It was tested that the PSFs did not vary over the field. The PSF images for the HST observations were constructed using Tiny Tim (Krist & Hook 1997) and have a size of 3″ × 3″.

All galaxies brighter than an apparent total magnitude in the I-band of $m_{\rm T} \approx 20^{\rm m}$ were fitted. The brightest cluster galaxies (BCG) in both clusters were fitted within a radius of 1-2$r_{\rm e}$. The fainter galaxies were fitted within the radius where the local surface brightness reached $\approx 26^{\rm m}$/arcsec^2 in the I-band. This radius is typically 5-7$r_{\rm e}$.

Before fitting the fainter galaxies the BCGs were modeled with the program Galphot (Franx, Illingworth & Heckman 1989a; Jørgensen, Franx & Kjærgaard 1992). This program fits a model of ellipses to the isophotes of the galaxy. The model was then subtracted. The use of Galphot ensures that gradients in the background due to signal from the BCG are properly removed before fitting the fainter galaxies. Further, the isophotes for the BCG in A2218 are not co-centric, as also noticed by Kneib et al. (1995). Galphot handles this properly while the fitting technique described above uses a fixed center and therefore leaves large residuals, which in turn affect the results for the fainter galaxies. The BCGs were also modeled with the 2-dimensional fitting technique. The effective radii derived from this agree within 0.02 in $\log r_{\rm e}$ with the results from fits to the growth curves produced by Galphot. Fitting the growth curves produced by Galphot does not give the possibility of 2-dimensional modeling the effect of the PSF. In the following, we therefore use results from the 2-dimensional fitting technique.

Table 4 lists the derived effective parameters. Only galaxies for which we also have spectroscopy are presented in this table. Tables A1 and A2 contain the derived effective parameters for all galaxies brighter than $19^{\rm m}$ and within

Table 4. Photometric parameters

		NOT						HST					
Galaxy	Field	$\log r_{\rm e}$ [arcsec]	$<\mu>_{\rm e}$ (I_c)	$\frac{\chi^2}{N_{\rm pix}}$	$<\mu>_{\rm e}$ (r_z)	$<\mu>_{\rm e}$ (V_z)	$(V-I_c)$	$\log r_{\rm e}$ [arcsec]	$<\mu>_{\rm e}$ (I_c)	$\frac{\chi^2}{N_{\rm pix}}$	$<\mu>_{\rm e}$ (r_z)	$<\mu>_{\rm e}$ (V_z)	$(V-I_c)$
A665-1150[a]	1	1.012	21.82	2.9	22.67	22.96	1.54	1.056	21.97	5.2	22.82	23.11	1.53
A665-1168	1	0.333	19.78	2.1	20.63	20.92	1.54	0.376	19.93	1.3	20.78	21.06	1.52
A665-1196	1	-0.352	17.73	9.0	18.58	18.86	1.51	-0.149	18.58	7.9	19.43	19.68	1.47
A665-2105[b]	2	0.876	22.09	29.7	22.92	23.07	1.20	1.003	22.42	18.5	23.23	23.41	1.24
A665-2108	2	-0.205	19.48	1.5	20.33	20.61	1.53	...	...	...	...	...	
A665-2111	2	-0.170	18.56	6.7	19.41	19.74	1.62	-0.011	19.17	4.1	20.02	20.29	1.51
A665-2144	2	-0.189	18.83	1.6	19.68	19.96	1.52	-0.096	19.22	1.6	20.06	20.29	1.41
A2218-L118	1	0.051	19.20	5.5	20.06	20.39	1.62	0.097	19.30	3.1	20.16	20.48	...
A2218-L148	1	-0.075	18.53	3.1	19.39	19.70	1.59	0.067	19.03	6.4	19.89	20.20	...
A2218-L198	1	-0.061	19.14	2.0	19.99	20.29	1.55	-0.143	18.81	1.9	19.67	19.96	...
A2218-L244	1	0.934	22.01	2.0	22.87	23.15	1.53	0.930	22.02	1.4	22.88	23.16	...
A2218-L341	1	-0.124	18.27	2.6	19.13	19.42	1.56	-0.116	18.26	4.1	19.11	19.41	...
A2218-L391[a]	1	1.403	23.07	3.6	23.92	24.18	1.48	1.412	23.25	21.0	24.10	24.37	...
A2218-L430	2	-0.033	19.06	1.4	19.92	20.24	1.62	-0.061	18.95	1.0	19.81	20.13	...
A2218-L482	2	0.036	18.77	2.2	19.63	19.95	1.62	...	...	...	...	...	
A2218-L535	2	0.238	19.63	1.9	20.49	20.82	1.63	...	...	...	...	...	

Notes. [a] Brightest cluster galaxy. [b] E+A galaxy. Identifications of galaxies in A2218 are from Le Borgne et al. (1992). Field – the NOT field that contains the galaxye, see Table 2 for seeing values. The observed magnitudes labeled I_c and V and the colors $(V-I_c)$ are standard calibrated to the Johnson-Kron-Cousins photometric system, and corrected for galactic extinction. The formal fitting uncertainties are typically as follows. $\log r_{\rm e}$: ±0.006 for NOT data, ±0.002 for HST data. $<\mu>_{\rm e}$: ±0.02 for NOT data, ±0.007 for HST data. The typical (random) uncertainty on the $(V-I_c)$ is 0.01. The goodness-of-fit is given as $\chi^2/N_{\rm pix}$, where $N_{\rm pix}$ is the number of pixels within the fitting radius. $\chi^2 = \sum(n_i - n_{i,\rm model})^2/\sigma_i^2$, with the sum over all the pixels within the fitting radius. n_i is the signal in pixel i, $n_{i,\rm model}$ is the model value in the pixel, and σ_i^2 the noise (photon- and read-out-noise) in the pixel.
Magnitudes r_z are fully corrected Gunn r magnitudes in the rest frames of the clusters, see equations (2) and (3). Magnitudes V_z are fully corrected Johnson V magnitudes in the rest frames of the clusters, see equations (4) and (5).

the fields covered by the NOT images. The magnitudes were standard calibrated as described in Appendix A. The I_c magnitudes from the HST data have been offset to consistency with the ground-based magnitudes, see Appendix A. Table 4 gives typical values of the formal fitting uncertainties. However, a comparison of the NOT and the HST data results in more realistic estimates of the uncertainties, see Appendix A. We find the uncertainties of $\log r_{\rm e}$ and $<\mu>_{\rm e}$ to be ±0.078 and ±0.29, respectively. Because of the correlation of the errors in $\log r_{\rm e}$ and $<\mu>_{\rm e}$, the combination $\log r_{\rm e} - 0.328<\mu>_{\rm e}$ that enters the FP has an uncertainty of only ±0.018. In the analysis of the FP for the clusters (Section 5), we use the average of the effective parameters determined from the HST observations and the NOT observations, whenever results from both telescopes are available.

2.2 Colors

The colors of the galaxies were determined from the ground-based observations. First, the I-band images were convolved to the seeing of the V-band images. This minimizes the errors in the derived colors due to mismatched seeing in the two passbands. The colors were derived within apertures with radii 1.″64 (10 pixels) and 2.″94 (18 pixels) for A665 and A2218, respectively. The larger aperture for A2218 was necessary due to the very poor seeing of the V-band images. The colors within these apertures are in the following used as global colors of the galaxies, see Table 4 for the sample that also has spectroscopy and Tables A1 and A2 for all galaxies brighter than $19^{\rm m}$. For nearby E and S0 galaxies, the color gradients in the local surface brightnesses are usually of the order $0^{\rm m}.05$ per dex in the radius, for colors based on Johnson B and Gunn r (e.g., Jørgensen et al. 1995a). The color gradients in the aperture magnitudes are smaller, typically less than $0^{\rm m}.04$ per dex in the radius. Assuming that the color gradients of the galaxies at redshift 0.18 are similar to those of nearby galaxies, the derived colors are expected to deviate less than ±0.02 from global colors within the effective radii. This results in a negligible effect of less than $0^{\rm m}.002$ on the calibrated magnitude in Gunn r in the rest frame of the clusters, cf. Sect. 2.3.

For the galaxies in A665 colors were also derived from the HST images. We used apertures with radii of 1.″5. The aperture size is smaller than those used for the NOT images in order to take advantage of the better spatial resolution of the HST images and limit the amount of contamination from neighboring objects. No correction for zero point offsets between the ground-based photometry and the HST photometry were applied to the colors, since we have no reliable way of checking the zero point for the HST V magnitudes. Thus, we implicitly assume that the zero point difference between the ground-based photometry and the HST photometry is the same in the I-band and the V-band. The colors derived from the HST observations are on average 0.04 mag bluer than the ground-based colors, cf. Table 4. This may be caused by errors in the HST colors due to the uncertainties in the magnitude zero points. Alternatively, uncertainties may be introduced by the poor seeing of the ground-based V images. The effect on the magnitudes calibrated to Gunn r in the rest frame of the cluster will be less than $0^{\rm m}.003$, cf. Sect. 2.3.

Table 5. Uncertainties affecting the photometric calibration

Cluster	Tel.	Calibration/Parameter	Random unc.	Systematic unc.
A665	NOT	Instrumental I_c		0.01
A2218	NOT	Instrumental I_c		0.015
A665,A2218	NOT	Standard I_c	0.021	
A665,A2218	NOT	Standard V	0.014	
A665,A2218	NOT	Standard $(V - I_c)$	0.025	
A665	HST	Holtzman et al. (1995) I_c	0.015	
A665	HST	Holtzman et al. (1995) $(V - I_c)$	0.028	
A665	HST	Offset to ground-based I_c		0.009
A2218	HST	Holtzman et al. (1995) I_c	0.017[a]	
A2218	HST	Offset to ground-based I_c		0.013
A665,A2218	NOT,HST	$(V - I_c)_{\rm meas}$ vs. $(V - I_c)_{r_{\rm e}}$	0.02	
A665,A2218	NOT	Total $(V - I_c)$	0.032	
A665	HST	Total $(V - I_c)$	0.034	
A665,A2218	NOT,HST	Gunn r in rest frame, transformation	0.02[b]	
A665,A2218	NOT,HST	Johnson V in rest frame, transformation	0.02[b]	
A665	NOT	Total r_z	0.028	0.01
A665	HST	Total r_z	0.024	0.02
A665	NOT	Total V_z	0.032	0.01
A665	HST	Total V_z	0.029	0.02
A2218	NOT	Total r_z	0.028	0.015
A2218	HST	Total r_z	0.024	0.028
A2218	NOT	Total V_z	0.032	0.015
A2218	HST	Total V_z	0.029	0.028

Notes. [a] Contributions from the transformation $(V - R_c) = 0.52(V - I_c)$ and the transformation from Holtzman et al. (1995). [b] Contribution from transformation, only.

2.3 Calibration to the rest frame of the clusters

In order to compare the FP for A665 and A2218 with results for nearby clusters we calibrate the photometry to Gunn r in the rest frame of the clusters. Following Frei & Gunn (1994), the magnitude in a broad passband can be written as $m_i = c_i - 2.5 \log F(\nu_i)$, with $c_i \equiv \Delta b_i - 48.60$. Δb_i are given by Frei & Gunn. $F(\nu_i)$ is the flux density at the effective wavelength of the passband. We assume the flux density in the redshifted Gunn r band is related to the observed V-band and I_c-band as $F(\nu_r(z)) = F(\nu_V)^\alpha F(\nu_{I_c})^{1-\alpha}$, cf. van Dokkum & Franx (1996). The magnitudes in Gunn r in the rest frame of the clusters can then be written

$$r_z = I_c + \alpha(V - I_c) - c_{\rm I_c} - \alpha(c_{\rm V} - c_{\rm I_c}) + c_{\rm r} + 2.5 \log(1+z) \quad (1)$$

where α is derived from the spectral energy distribution. The I_c magnitudes and the colors $(V - I_c)$ are the observed standard calibrated values, corrected for galactic extinction.

A665 has z=0.181 (Oegerle et al. 1991). From the spectral energy distributions for E and Sa galaxies given by Coleman, Wu & Weedman (1982) we find $\alpha_{\rm A665} = 0.053$. The resulting calibration to reach Gunn r in the rest frame is

$$r_z = I_c + 0.053(V - I_c) + 0.77 \quad (2)$$

A2218 has z=0.176 (Le Borgne, Pelló & Sanahuja 1992). We find $\alpha_{\rm A2218} = 0.062$, and the resulting calibration is

$$r_z = I_c + 0.062(V - I_c) + 0.76 \quad (3)$$

The mean surface brightnesses, $<\mu>_{\rm e}$, calibrated to Gunn r in the rest frame of the clusters are given in Table 4.

Table 4 also lists the mean surface brightnesses calibrated to Johnson V in the rest frame of the clusters. The calibrations to reach Jonhson V are

$$V_z = I_c + 0.48(V - I_c) + 0.40 \quad (4)$$

for A665 and

$$V_z = I_c + 0.49(V - I_c) + 0.39 \quad (5)$$

for A2218.

Because the photometry for the best comparison sample (the Coma cluster) is available in Gunn r, and also because of the uncertainty in the derived colors, cf. Section 2.2, we will primarily use the mean surface brightnesses calibrated to Gunn r throughout the rest of this paper.

2.4 Summary of uncertainties

Table 5 summarizes the different sources on uncertainty affecting the photometric calibration. The entries noted as "Total" uncertainty give the total uncertainty on the listed parameter, while all other entries give the contribution from the individual calibration step. The uncertainties on the instrumental I_c magnitudes for the NOT data refer to the consistency of the magnitude zero points of the co-added images, cf. Sect. A1. The uncertainties on the standard calibrated magnitudes for the NOT data are the rms scatter of the standard transformations, cf. Sect. A3. For the HST data the uncertainties consist of random uncertainties due to the uncertainties in the transformations adopted from Holtzman et al. (1995), cf. Sect. A3, and systematic uncertainties in matching the HST photometry to the ground-based system. The colors $(V - I_c)$ are subject to an additional uncertainty because we measure the colors within fixed aperture sizes rather than within the effective radii, cf. Sect. 2.2. Finally, the transformations used to calibrate the magnitudes to Gunn r and Johnson V in the rest frames of the clusters contribute to the uncertainties. The last part of Table

5 summarizes the total uncertainties, random or systematic, on the calibrated magnitudes r_z and V_z. The magnitudes have typical random uncertainties of $0\overset{m}{.}03$, and typical systematic uncertainties of $0\overset{m}{.}02$.

3 THE SPECTROSCOPY

A665 galaxies were selected for the spectroscopic observations from a ground-based R-band image kindly provided by M. Birkinshaw. The flux of the galaxies within a $1\overset{''}{.}8 \times 8''$ aperture was used as selection criterion. Spectra of 7 galaxies in A665 were obtained with the MMT in January 1991, cf. Table 1. The total integration time was 9 hours. For one of the galaxies the signal-to-noise was too low to derive a reliable value of the velocity dispersion.

For A2218 we used the catalog by Le Borgne, Pelló & Sanahuja (1992) as the main source for the selection of galaxies, supplemented with the catalog by Butcher, Oemler & Wells (1983). Galaxies were selected on magnitude and color. The $(B-R)$ color was required to be within 0.15 of the color-magnitude relation for the red cluster galaxies. One redder galaxy, BOW97, was included. This galaxy turned out to be a background galaxy. Spectra of 10 galaxies in A2218 were obtained with the KPNO 4m in June 1994, cf. Table 1. The total integration time was 11.8 hours.

The basic reductions of the spectroscopy are described in Appendix B, which also shows the final spectra of the galaxies. Here we describe the determination of the velocity dispersions (see also Franx 1993ab for the galaxies in A665).

3.1 Instrumental resolution and template stars

Determination of velocity dispersions of galaxies is usually done with spectra of template stars obtained with the same instrumentation as the galaxy spectra. Due to the large redshifts of A665 and A2218 this will not work for these clusters. A further complication is that the spectra of A665 and A2218 were obtained through multi-slit masks and the instrumental resolution varies with wavelength and from slit-let to slit-let.

Following van Dokkum & Franx (1996), we mapped the instrumental resolution from He-Ne-Ar lamp exposures. Further, the instrumental resolution was determined from the sky lines in the final average spectra of the galaxies. In all cases Gaussian profiles were fitted to the emission lines. Fig. 1 shows the instrumental resolution versus wavelength for representative slit-lets for the A2218 spectra. The determinations from lamp exposures and from sky lines agree. Low order polynomials were fitted to the instrumental resolution versus wavelength for each slit-let.

We used a spectrum of HD192126 as the template star for the A665 spectra. The spectrum of the star was obtained with the Canada-France-Hawaii Telescope by K. Kuijken. The wavelength range for the spectrum is 4650-5650Å, with a resolution of $\sigma_{\rm inst} = 0.56$Å. As template stars for the A2218 spectra we used spectra of HD56224, HD72324 and HD102494 obtained with the Keck Telescope in May 1996 by D. Kelson. The wavelength range of these spectra is 4002-5314Å, with a resolution of $\sigma_{\rm inst} = 0.9$Å.

For each galaxy spectrum the spectra of the template stars were convolved to the instrumental resolution of the

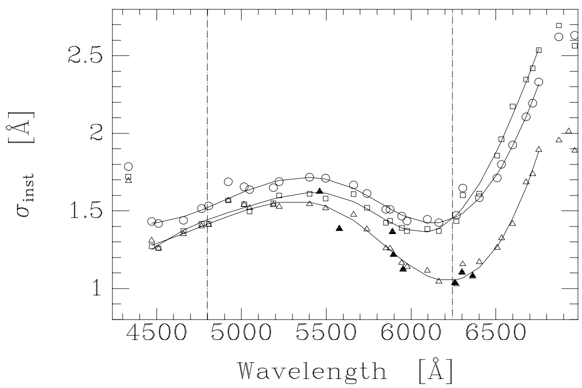

Figure 1. The instrumental resolution for the A2218 spectra, as derived from He-Ne-Ar calibration spectra. Triangles – central slit-let; boxes and circles – the two slit-lets closest to the edges of the CCD. The filled symbols are based on sky lines. The resolution derived from the sky lines agree with the resolution derived from the calibration spectra. The solid lines show the fitted functions. The dot-dashed lines show the approximate wavelength interval, which was used for determination of the velocity dispersions.

galaxy spectrum. The variation of the resolution with wavelength was taken into account.

3.2 Fourier Fitting

The velocity dispersions, σ, were determined by fitting the galaxy spectra with the template spectra using the Fourier Fitting Method (Franx, Illingworth & Heckman 1989b). The Fourier transforms of the spectra were filtered to avoid the low frequencies. We used a limit equivalent to $\approx$(100Å)$^{-1}$ in the rest frame of the clusters. This is the same limit used by Jørgensen, Franx & Kjærgaard (1995b). In the case of A2218, the final velocity dispersion is the average of the determinations with the three different template stars. The formal fitting uncertainty on $\log \sigma$ is typically 0.023. For A665 the mean spectra over the central $1\overset{''}{.}8$ were fitted. Thus, the aperture size is $1\overset{''}{.}8 \times 1\overset{''}{.}8$. The aperture size used for A2218 was $1\overset{''}{.}9 \times 3\overset{''}{.}45$.

For the A2218 galaxies we experimented with fitting the spectra in a limited wavelength range around the G-band region (rest frame 4080-4700Å) and around the Mgb region (rest frame 4800-5310Å), as well as the full available wavelength range (rest frame 4080-5310Å). Fig. 2 shows the comparison of the velocity dispersions derived from the G-band region and from the Mgb region. The median offset in $\log \sigma$ is 0.00 ± 0.02. In the following the results from fitting the full wavelength range are used.

The velocity dispersions were aperture corrected to a circular aperture with diameter $1.19\,h^{-1}$ kpc, equivalent to 3.4 arcsec at the distance of the Coma cluster. We adopt the technique for the aperture correction established by Jørgensen et al. (1995b). The applied aperture corrections are 0.0215 and 0.028 in $\log \sigma$ for A665 and A2218, respectively. Table 6 gives the raw determinations of the velocity dispersions as well as the aperture corrected values.

The velocity dispersion measurements for A665 and A2218 are based on two independent observing runs. Fur-

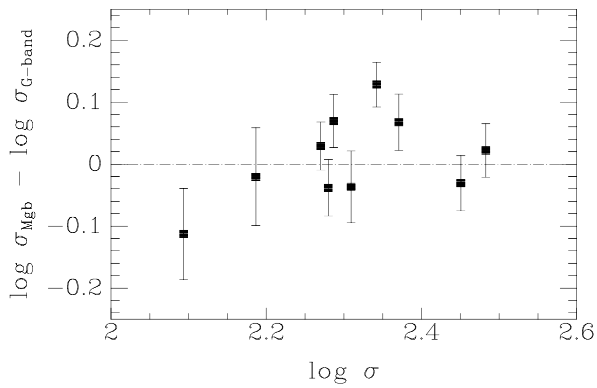

Figure 2. The difference between velocity dispersions derived from the Mgb region (rest frame 4800-5310Å) and from the G-band regon (rest frame 4080-4700Å) versus the velocity dispersions derived from the full wavelength range. Only data for galaxies in A2218 are shown. The median offset in $\log\sigma$ is 0.00 ± 0.02.

ther, in the analysis (Sect. 5) we will use the data together with measurements from other independent observing runs. We have no way of testing the consistency of the velocity dispersion measurements from the different runs, since there are no galaxies in common between the runs. For nearby galaxies (redshifts less than 0.1) it is in general found that velocity dispersion measurements from different runs can deviate with 0.01 to 0.025 in $\log\sigma$ (e.g., JFK1995b; Smith et al. 1997; Wegner et al. 1998). We adopt the mean offset of 0.023 in $\log\sigma$ found by Wegner et al. in their analysis of 33 observing runs to be the typical systematic uncertainty for velocity dispersion measurements from independent observing runs. The uncertainty on the applied aperture correction is expected to be significantly smaller than this systematic uncertainty.

4 DATA FOR OTHER CLUSTERS

4.1 The Coma cluster and the HydraI cluster

The Coma cluster is in the following used as the low redshift reference for our study of changes in the FP as a function of the redshift. We use the sample of E and S0 galaxies, which has photometry in Gunn r from Jørgensen et al. (1995a), see also Jørgensen & Franx (1994). The sample covers the central $64' \times 70'$ of the cluster. Velocity dispersions published by Davies et al. (1987), Dressler (1987), and Lucey et al. (1991) have been calibrated to a consistent system and aperture corrected to a circular aperture with diameter 1.19 h^{-1} kpc, equivalent to 3.4 arcsec at the distance of the Coma cluster, see Jørgensen et al. (1995b). Further, we use new velocity dispersion measurements from Jørgensen (1999). A total of 116 galaxies have available photometry and spectroscopy. The sample is 93% complete to a magnitude limit of $m_{\rm T} = 15\overset{\rm m}{.}05$ in Gunn r, equivalent to $M_{\rm r_T} = -20\overset{\rm m}{.}75$ (for a distance modulus of $35\overset{\rm m}{.}8$, $H_0 = 50\ {\rm km\,s^{-1}\,Mpc^{-1}}$ and $q_{\rm o} = 0.5$).

For the purpose of testing for possible differences in the coefficients of the FP we have also used data for galaxies in the HydraI cluster. The main purpose of including the HydraI cluster is to add more high luminosity galaxies to the nearby sample. We use the sample of E and S0 galaxies by Milvang-Jensen & Jørgensen (1999). The sample covers the central $68' \times 83'$ of the cluster. A total of 45 galaxies have photometry (in Gunn r) and spectroscopy. The sample is 80% complete to $m_{\rm T} = 14\overset{\rm m}{.}5$ in Gunn r (equivalent to $M_{\rm r_T} = -20\overset{\rm m}{.}0$, for a distance modulus of $34\overset{\rm m}{.}5$). For the galaxies brighter than $M_{\rm r_T} = -20\overset{\rm m}{.}75$, the FP for the HydraI cluster is the same as for the Coma cluster.

Table 6. Spectroscopic parameters

Galaxy	$\log\sigma$ (obs)	$\log\sigma$ ($3\overset{''}{.}4$)	$\sigma_{\log\sigma}$	z	S/N
A665-1150	2.447	2.468	0.019	0.1831	54.5
A665-1168	2.356	2.378	0.019	0.1785	54.5
A665-1196	2.334	2.355	0.028	0.1691	32.6
A665-2105	2.127	2.149	0.035	0.1699	40.7
A665-2108	...	...	...	0.1939	16.5
A665-2111	2.369	2.391	0.025	0.1860	37.2
A665-2144	2.267	2.288	0.034	0.1729	29.4
A2218-L118	2.280	2.308	0.023	0.1748	32.2
A2218-L148	2.371	2.399	0.023	0.1833	27.6
A2218-L198	2.309	2.337	0.027	0.1737	22.4
A2218-L244	2.287	2.315	0.020	0.1772	32.2
A2218-L341	2.451	2.479	0.023	0.1630	25.2
A2218-L391	2.483	2.511	0.022	0.1731	38.1
A2218-L430	2.093	2.121	0.035	0.1810	21.7
A2218-L482	2.342	2.370	0.018	0.1788	35.2
A2218-L535	2.270	2.298	0.021	0.1809	31.1
A2218-BOW33	2.186	2.214	0.038	0.1734	18.2
A2218-BOW97	...	...	...	0.291	12.7

Notes. (obs) – raw measurements. ($3\overset{''}{.}4$) – aperture corrected to a circular aperture with diameter 1.19 h^{-1} kpc, equivalent to $3\overset{''}{.}4$ at the distance of the Coma cluster. $\sigma_{\log\sigma}$ – formal uncertainty from the Fourier Fitting Method. S/N – signal-to-noise per Ångström in the wavelength interval used for the Fourier fitting. Identifications for A2218 are from Le Borgne et al. (1992) and Butcher et al. (1983).

4.2 Intermediate redshift clusters

In the following analysis we also use data for the three intermediate redshift clusters CL0024+16 (van Dokkum & Franx 1996), CL1358+62 and MS2053-04 (Kelson et al. 1997). Van Dokkum & Franx and Kelson et al., who previously studied these clusters, give effective radii, magnitudes V_z calibrated to the V-band in the rest frame of the clusters, colors, and velocity dispersions. We establish the transformations from the observed I_c magnitudes and $(R_c - I_c)$ to Gunn g in the rest frames of the clusters, using the technique described in Section 2.3. We then use the relation $(V - g) = -0.517(g - r) - 0.027$ (Jørgensen 1994), based on standard stars, to transform $(V_z - g_z)$ to $(g_z - r_z)$, where g_z and r_z are Gunn g and Gunn r, respectively, in the rest frames of the clusters. This results in calibrations that allow us to transform from the published magnitudes V_z and the color $(R_c - I_c)$ to Gunn r in the rest frames of the clusters. For CL0024+16 at a redshift of 0.39 we find

$$V_z - r_z = 0.58(R_c - I_c) - 0.21 \qquad (6)$$

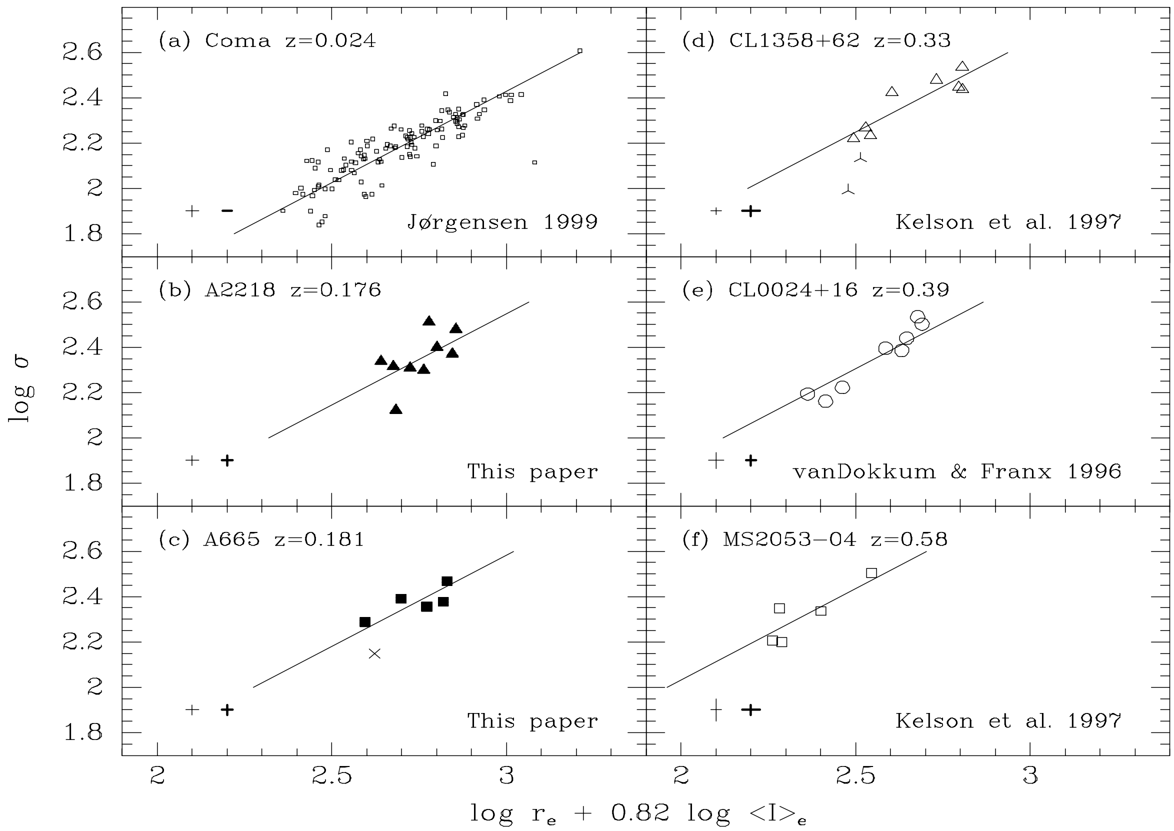

Figure 3. The FP edge-on for Coma, A2218, A665, CL1358+62, CL0024+16, and MS2053-04. The sources of the data are given on the panels. The skeletal symbols on panel (c) and (d) are the E+A galaxies. The photometry is calibrated to Gunn r in the rest frames of the clusters. The mean surface brightness $\log \langle I\rangle_{\rm e} = -0.4(\langle\mu\rangle_{\rm e} - 26.4)$ is in units of $L_\odot/{\rm pc}^2$. The photometry is not corrected for the dimming due to the expansion of the Universe. The effective radii are in kpc ($H_0 = 50$ km s^{-1} Mpc^{-1} and $q_{\rm o} = 0.5$). The solid lines are the FPs with coefficients adopted from JFK96 and zero points derived from the data presented in the figure. Typical error bars are given on the panels; the thin and thick error bars show the random and systematic uncertainties, respectively.

For CL1358+62 at $z = 0.33$ we find

$$V_z - r_z = 0.50(R_c - I_c) - 0.19 \quad (7)$$

The data for CL1358+62 include two E+A galaxies (Kelson et al.). For MS2053-04 at $z = 0.58$ we find

$$V_z - r_z = 0.30(R_c - I_c) - 0.15 \quad (8)$$

The uncertainties on r_z derived using these transformations consist of the uncertainty due to the transformation between $(V - g)$ and $(g - r)$ (0.015) and the uncertainty due to the transformation to g_z ($0\overset{\rm m}{.}02$), a total of $0\overset{\rm m}{.}025$. We do not include additional uncertainty from the authors' original transformation to V_z since that uncertainty is closely correlated with the uncertainty on the transformation to g_z. The uncertainty of $0\overset{\rm m}{.}025$ does not include the uncertainties in the standard calibrations to I_c and R_c established by van Dokkum & Franx and Kelson et al.

The typical values of $V_z - r_z$ derived from equations (6) to (8) are 0.2. This is comparable to the average $(V-r)$ color of nearby E and S0 galaxies (e.g, Jørgensen et al. 1995a). Others found similar small color evolution for E galaxies in clusters with redshifts less than 0.6, e.g., Rakos & Schombert (1995) who used passbands shifted to match the redshift of the studied clusters.

5 THE FUNDAMENTAL PLANE

Fig. 3 shows the FP edge-on for A665 and A2218 as $\log\sigma$ versus $\log r_{\rm e} + 0.82 \log \langle I\rangle_{\rm e}$. The mean surface brightness $\log \langle I\rangle_{\rm e} = -0.4(\langle\mu\rangle_{\rm e} - 26.4)$ is in units of $L_\odot/{\rm pc}^2$. The figure also shows the FP for the Coma cluster and for the three intermediate redshift clusters CL1358+62 ($z = 0.33$), CL0024+16 ($z = 0.39$) and MS2053-04 ($z = 0.58$). The E+A galaxies in A665 and CL1358+62 are excluded from the following analysis, but are shown on the figures.

We adopt the coefficients for the FP from JFK96, $(\alpha,\beta)=(1.24 \pm 0.07, -0.82 \pm 0.02)$. The coefficients were derived for a sample of 226 galaxies in 10 nearby clusters. Photometry in Gunn r was used. The relations shown on Fig. 3 are FPs with these coefficients.

The error bars on Fig. 3 showing the systematic errors include the systematic uncertainties in the photometry (cf. Table 5) and a 2% systematic uncertainty in $r_{\rm e}\langle I\rangle_{\rm e}^{0.82}$ due to any deviations from $r^{1/4}$ profiles and possible differences

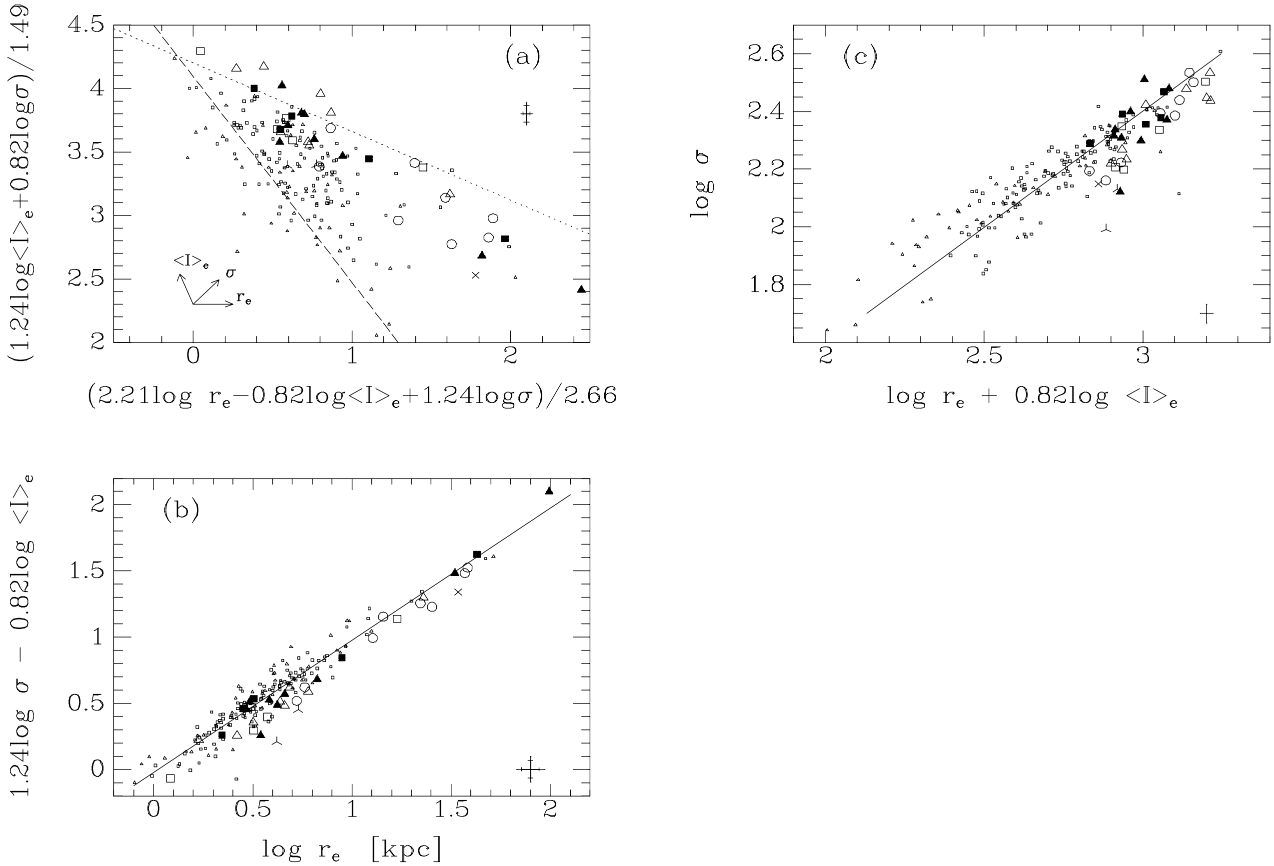

Figure 4. The FP for Coma, HydraI and the five intermediate redshift clusters. Small triangles – galaxies in HydraI; other symbols as on Fig. 3. The photometry is calibrated to Gunn r in the rest frames of the clusters and corrected for the dimming due to the expansion of the Universe. The effective radii are in kpc. $H_0 = 50$ km s^{-1} Mpc^{-1} and $q_o = 0.5$ were used. (a) The FP face-on. The dashed line marks the luminosity limit for the completeness of the Coma cluster sample, $M_{\rm r_T} = -20^{\rm m}_{.}75$. The dotted line is the so-called exclusion zone for nearby galaxies, $y \approx -0.54x + 4.2$, first noted by Bender et al. (1992). (b) and (c) The FP edge-on. The solid line is the FP for the Coma cluster with coefficients adopted from JFK96. The small error bars on panels (a) and (b) refer to Coma and HydraI, while the larger error bars refer to the intermediate redshift clusters. The error bars on panel (c) refer to Coma and HydraI. The error bars for the intermediate redshift clusters cannot be summarized in a simple fashion, and we refer to Fig. 3 for their sizes.

originating from differences in the fitting methods for the nearby and intermediate redshift galaxies (cf. Kelson et al. 1997). The systematic uncertainties on $\log\sigma$ is shown as 0.023 for the intermediate redshift clusters and zero for the Coma cluster, since the relevant uncertainty is the possible inconsistency between the velocity dispersions for Coma galaxies and the intermediate redshift galaxies.

Fig. 4 shows the FP face-on and in two edge-on views. The HydraI sample is included on this figure. The mean surface brightnesses have been corrected for the dimming due to the expansion of the Universe. The effective radii are in kpc ($H_0 = 50$ km s^{-1} Mpc^{-1} and $q_o = 0.5$).

The scatter around the FP is similar for A665 and A2218 (0.060 and 0.112 in $\log r_{\rm e}$) and for the Coma cluster (0.092 in $\log r_{\rm e}$). Using the photometry calibrated to Gunn r, we find the scatter for CL1358+62, CL0024+16 and MS2053-04 to be 0.066, 0.064 and 0.076, respectively (see also van Dokkum & Franx 1996; Kelson et al. 1997). This is not significantly different from the scatter for Coma, A665 and A2218. The scatter for the Coma cluster reported here is somewhat larger than previous estimates based on smaller samples (e.g., Jørgensen et al. 1993, 1996; Lucey et al. 1991).

5.1 The coefficients of the FP

The sample of intermediate redshift galaxies is heavily biased towards intrinsically bright galaxies. The faintest galaxies observed in the intermediate reshift clusters typically have $M_{\rm r_T} = -21^{\rm m}_{.}65$. The selection effect is clearly visible in the face-on view of the FP, Fig. 4a. Further, the edge-on view on Fig. 4c shows that the samples are limited in both the velocity dispersions and in $\log r_{\rm e} + 0.82 \log \langle I \rangle_{\rm e}$. The selection effects make it difficult to test for possible differences between the coefficients of the FP for Coma and the FP for the intermediate redshift clusters.

Fig. 5a shows the FP as the relation between the M/L ratio and the mass. The masses were derived as $M = 5 r_{\rm e} \sigma^2 / G$ (cf., Bender, Burstein & Faber 1992). This figure and Fig. 4c indicate that the coefficient α for the $\log\sigma$ term in the FP is different for the intermediate redshift clusters and for the Coma cluster. This was also noted by van

Dokkum & Franx (1996) in their analysis of the CL0024+16 observations.

We tried to fit the FP to the intermediate redshift clusters individually, in order to test if the coefficients of the FP for the intermediate redshift clusters are different from those for nearby clusters. A total of 35 galaxies were included in the fits. The E+A galaxies in A665 and CL1358+62 were omitted, since we aim at fitting the FP for the E and S0 galaxies, only. The fits were determined by minimization of the sum of the absolute residuals perpendicular to the relation. The uncertainties were derived using a bootstrap method (cf., JFK96). All the fits gave β values in the interval -0.75 to -0.81. The α values are in the interval 0.54–1.74 and, due to the small sample sizes, the uncertainties are large. We therefore repeated the fits with $\beta = -0.79$ for all the clusters. This gives α in the interval 0.45–1.42, with uncertainties of 0.14–0.70. No significant change of α with redshift was detected. It must await larger samples of galaxies to map the possible change of the coefficients as a function of the redshift.

Next, we fit the FP to the five clusters as parallel planes, under the assumption that the FPs for these clusters have the same coefficients. For the photometry calibrated to Gunn r, this gives $(\alpha,\beta)=(0.89\pm0.17,-0.79\pm0.04)$. In Johnson V we find $(\alpha,\beta)=(0.92\pm0.13,-0.79\pm0.04)$. A fit to the Coma cluster galaxies alone gives $(\alpha,\beta)=(1.27\pm0.08,-0.81\pm0.03)$, for photometry in Gunn r. The difference between α for the Coma cluster sample and α for the intermediate redshift sample is 0.38. Of the 1000 bootstrap fits derived for the FP for the intermediate redshift sample, 3.8 percent have α values that deviate from $\alpha = 0.89$ with more than 0.38. Hence, the difference in α is significant at the 96 percent level.

In order to explore the effect of the different selection criteria we repeated the fit to the Coma cluster galaxies first enforcing a magnitude limit of $M_{\rm r_T} = -21\overset{\rm m}{.}65$, and next enforcing limits of $\log\sigma \geq 2.12$ and $\log r_{\rm e} + 0.82\log <I>_{\rm e} \geq 2.80$. Applying the magnitude limit, does not give a result significantly different from the fit for the full sample, we find $(\alpha,\beta)=(1.30\pm0.17,-0.82\pm0.06)$. The limits in $\log\sigma$ and $\log r_{\rm e} + 0.82\log <I>_{\rm e}$ result in $(\alpha,\beta)=(1.09\pm0.27,-0.85\pm0.05)$. Though this is formally not different from the fit to the full sample, the smaller value of the α coefficient indicates that part of the difference in α between the Coma cluster sample and the sample in the intermediate redshift clusters may be due to selection effects.

To further test if the difference in α may be due to selection effects, we have performed two simulations that are both based on fitting the FP to random sub-samples of galaxies selected from the Coma cluster sample plus the HydraI cluster sample. The sub-samples each contain 35 galaxies in order to match the size of the intermediate redshift sample. In the first simulation, the sub-samples were selected such that their luminosity distributions match the luminosity distribution for intermediate redshift cluster sample. In the second simulation, the sub-samples were selected to match the distribution of $\log r_{\rm e} + 0.82\log <I>_{\rm e}$. The mean luminosity evolution of the galaxies in the intermediate redshift clusters (see Section 5.2) was taken into account in both simulations. However, the results do not depend on whether this correction is applied.

We have included the HydraI cluster sample in these

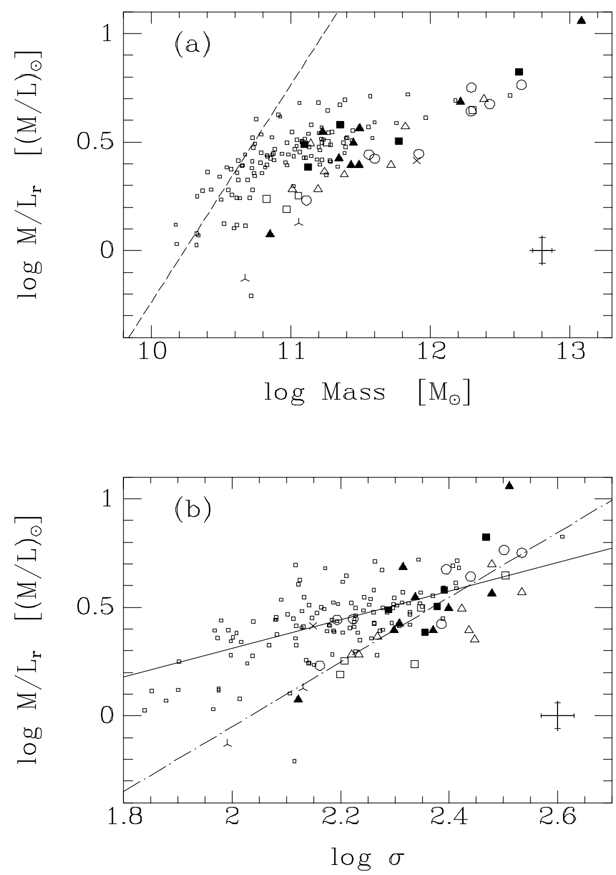

Figure 5. (a) The M/L ratio as function of the mass. The dashed line marks the luminosity limit for the completeness of the Coma cluster sample, $M_{\rm r_T} = -20\overset{\rm m}{.}75$. (b) The M/L ratio as function of the velocity dispersion. Solid line – relation fitted to the Coma cluster; dotted-dashed line – relation fitted to the intermediate redshift clusters. Symbols as in Fig. 3. The small and large error bars refer to the random uncertainties affecting the Coma cluster and the intermediate redshift clusters, respectively.

simulations because the Coma cluster sample has only six galaxies brighter than $M_{\rm r_T} = -23^{\rm m}$. Our sample of galaxies in the intermediate redshift clusters include 13 galaxies brighter than $M_{\rm r_T} = -23^{\rm m}$. Thus, using only the Coma cluster sample for the test could potentially bias the result, since the bright galaxies would appear several times in each sub-sample. The combined Coma and HydraI sample contains 10 galaxies brighter than $M_{\rm r_T} = -23^{\rm m}$. While this may not be enough to eliminate all bias due to some of the bright galaxies being included more than once in each sub-sample, we expect the bias to be fairly small.

Figs. 6a and c show the distribution of α values for 1000 random sub-samples for each of the two simulations. The values for the full Coma cluster sample and for the intermediate redshift sample are overplotted. Eight (0.8 percent) of the sub-samples selected to match the luminosity distribution result in values of α within the one sigma error bar of the coefficient found for the intermediate redshift sample. For the sub-samples selected to match the distribution in

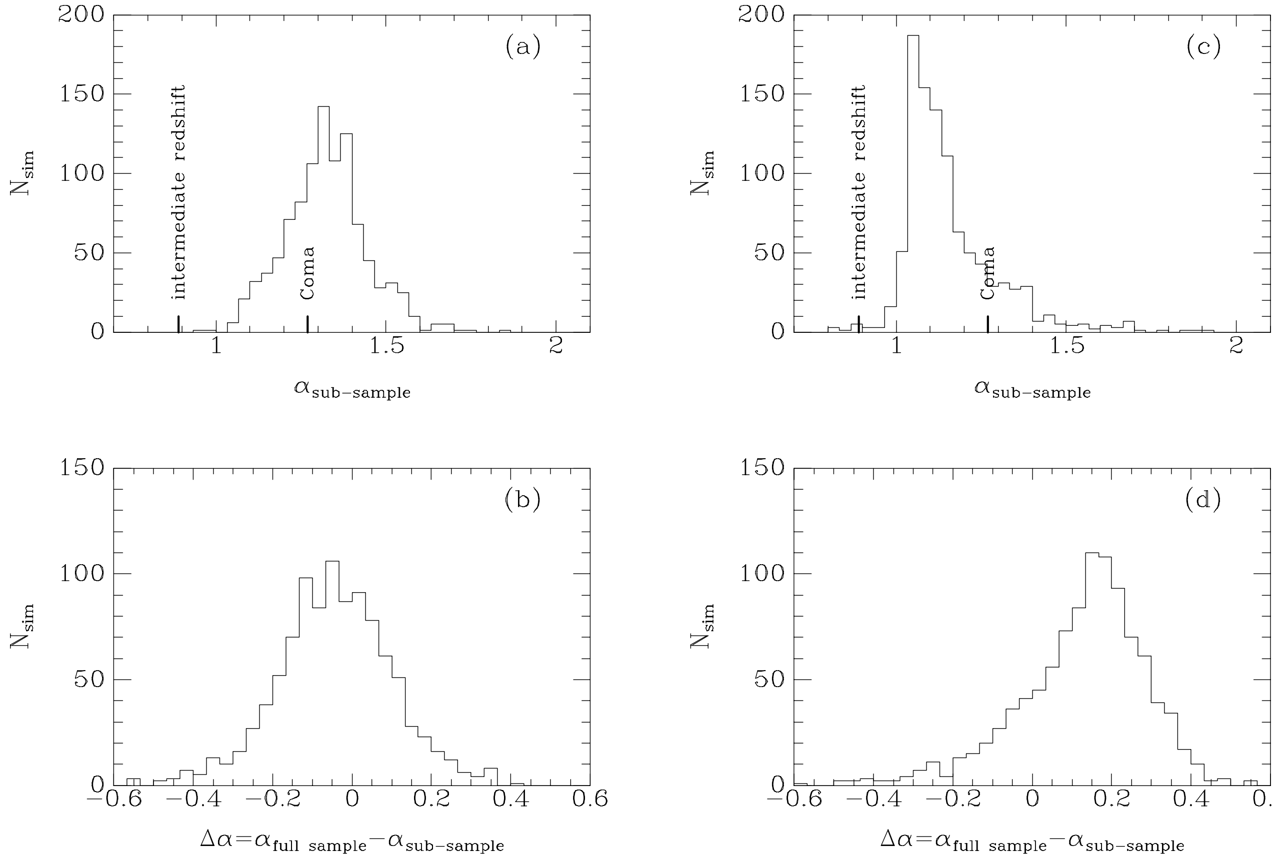

Figure 6. (a) Histogram of the values of the coefficient α of the FP for 1000 random sub-samples of galaxies selected from the Coma cluster and HydraI cluster sample. The sub-samples are selected so their luminosity distributions match the luminosity distribution for the intermediate redshift sample. The values found for the intermediate redshift sample and for the full Coma cluster sample are also shown. (b) Histogram of the difference between the α values derived by bootstrapping the full Coma sample and the α values derived from the random sub-samples selected to match the luminosity distribution. The absolute difference $|\Delta\alpha|$ is larger than 0.38 for 1.8 percent of the cases. (c) Histogram of the values of the coefficient α of the FP for 1000 random sub-samples of galaxies selected from the Coma cluster and HydraI cluster sample. The sub-samples are selected so their distribution in $\log r_{\rm e} + 0.82 \log \langle I\rangle_{\rm e}$ match the distribution for the intermediate redshift sample. The values found for the intermediate redshift sample and for the full Coma cluster sample are also shown. (b) Histogram of the difference between the α values derived by bootstrapping the full Coma sample and the α values derived from the random sub-samples selected to match the distribution in $\log r_{\rm e} + 0.82 \log \langle I\rangle_{\rm e}$. The absolute difference $|\Delta\alpha|$ is larger than 0.38 for 3.8 percent of the cases.

$\log r_{\rm e} + 0.82 \log \langle I\rangle_{\rm e}$, 20.3 percent give α values within the one sigma error bar.

The distributions of the β values for the sub-samples encompass for both simulations the value for the Coma cluster sample as well as the value for the intermediate redshift sample, which in turn are not significantly different from each other.

In order to construct two-sided tests, we compare the α values derived from the two simulations of the sub-samples to those derived by bootstrapping the full Coma sample. The comparison with the first simulation gives a measure of how often we can expect two samples with luminosity distributions similar to the intermediate redshift sample and the Coma cluster sample, respectively, and drawn from the same underlying distribution, to give a difference in α larger than the measured difference of 0.38. The comparison with the second simulation gives the same measure for samples selected on the distribution in $\log r_{\rm e} + 0.82 \log \langle I\rangle_{\rm e}$. Fig. 6b and d show the distributions of the α difference for the two comparisons. For the sub-samples selected to match the luminosity distribution, 18 of the 1000 cases, or 1.8 percent, have an absolute difference $|\Delta\alpha|$ larger than 0.38. For the sub-samples selected to match the distribution in $\log r_{\rm e} + 0.82 \log \langle I\rangle_{\rm e}$, 3.8 percent of the cases have $|\Delta\alpha| > 0.38$.

Based on these simulations, we conclude that the difference in the α coefficient of the FP is not likely to be due to the difference in the luminosity distributions of the two samples. It is possible that part of the difference in the α coefficient is due to the distribution of $\log r_{\rm e} + 0.82 \log \langle I\rangle_{\rm e}$ being different for the two samples. The different appearances of the distributions shown on Figs. 6a and c add to the evidence that the selection effect present in $\log r_{\rm e} + 0.82 \log \langle I\rangle_{\rm e}$ may affect the derived value of α.

The coefficients we find for the FP for the intermediate redshift clusters imply that

$$M/L \propto {r_{\rm e}}^{0.27} \sigma^{0.87} \propto M^{0.44} {r_{\rm e}}^{-0.17} \qquad (9)$$

Table 7. Uncertainties on the FP zero point

Source	Clusters Coma	A665	A2218	random/systematic
Photometric zero point $\sigma(<\mu>_e)$	0.015	0.02	0.02	systematic
Velocity dispersion	0.000	0.023	0.023	systematic
Coma peculiar velocity, 300km/s, $\sigma(\log r_e)$	0.018	...	...	systematic
Total systematic uncertainty, $\sigma(\log r_e)$	0.023	0.035	0.035	systematic
Uncertainty on the FP zero point[a], $\sigma(\log r_e)$	0.009	0.027	0.037	random

Note. The uncertainty on the FP zero point is $\sigma_{\rm fit}/N^{1/2}$ where $\sigma_{\rm fit}$ is the rms scatter of the FP and N is the number of observed galaxies.

This should be compared with $M/L \propto {r_e}^{0.22}\sigma^{0.49} \propto M^{0.24}{r_e}^{-0.02}$ found for nearby clusters (JFK96). The difference may indicate that the low mass galaxies show a stronger luminosity evolution than the more massive galaxies. The driving factor may however be the velocity dispersion rather than the mass of the galaxies. A direct fit to the M/L ratio as a function of the velocity dispersion gave for the nearby clusters $M/L \propto \sigma^{0.86}$ (JFK96). Fig. 5b shows the M/L ratio versus the velocity dispersion for the Coma cluster and the intermediate redshift clusters. The different slopes for the two samples is clearly seen. For the Coma cluster alone we find $M/L \propto \sigma^{0.66\pm0.13}$, while the sample of galaxies in the intermediate redshift clusters gives $M/L \propto \sigma^{1.49\pm0.29}$. The relations for the Coma cluster and for the intermediate redshift clusters are overplotted on Fig. 5b.

If real, the difference in the slopes of the FP (and the slopes of the M/L-σ relation) may be due to bursts of star formation in the low mass galaxies in the intermediate redshift clusters leading to a lower M/L ratio for these galaxies. Alternatively, the samples in the intermediate redshift clusters may contain some early-type spirals.

5.2 The evolution of the M/L ratio

The zero point of the FP depends on the cosmological effects (surface brightness dimming, the value of q_o, and the value of the cosmological constant), and the evolution of the galaxies. We assume a cosmological constant of zero. We adopt the coefficients for the FP for nearby clusters (JFK96) for all the clusters. Because of the possible difference in the coefficients of the FP (cf. Section 5.1) the following discussion of the evolution of the M/L ratios should be understood as the average evolution of the available samples of galaxies. Specifically, the results refer to galaxies with masses above $6.5 \cdot 10^{10} M_\odot$ ($H_0 = 50$ km s^{-1} Mpc^{-1} and $q_o = 0.5$).

Table 7 summarizes the sources of uncertainty affecting the zero points of the FP for Coma, A665 and A2218. The total systematic uncertainty on the FP zero point is the sum of the systematic uncertainties and is given as $\sigma(\log r_e)$. The random uncertainties introduced by the random photometric uncertainties and fitting uncertainties are included in the uncertainty on the FP zero point since this is based on the measured rms scatter of the FP.

On the following figures the error bars reflect the uncertainties listed in Table 7. The uncertainties for the other intermediate redshift clusters were adopted from van Dokkum & Franx (1996) and Kelson et al. (1997), and where necessary the total uncertainties were derived in the same way as for A665 and A2218.

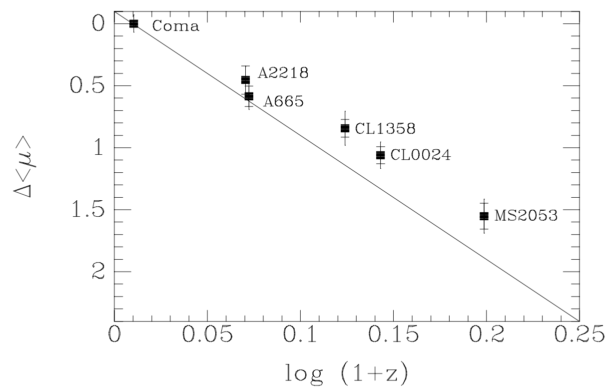

Figure 7. The offsets in the surface brightnesses derived from the FP versus the redshift of the clusters. $q_o = 0.5$ was used. The small and large error bars show the random and systematic uncertainties, respectively. These were derived as $\sigma(<\mu>_e) = \sigma(\log r_e) \cdot 2.5/0.82$. See Table 7 for values of $\sigma(\log r_e)$. The solid line is the expected relation for an expanding Universe and no evolution of the galaxies. The data are in agreement with an expanding Universe and a slow luminosity evolution. A smaller q_o results in smaller values of $\Delta<\mu>$, and therefore a larger luminosity evolution.

Fig. 7 shows the offsets in the surface brightnesses, $\Delta<\mu>$, based on the zero points of the FPs. We used $q_o = 0.5$. No correction for the expansion of the Universe has been applied and the solid line on the figure shows the expected relation for an expanding Universe. A smaller q_o results in smaller values of $\Delta<\mu>$. The data are consistent with an expanding Universe and a slow luminosity evolution of the galaxies. In the following we correct the data for the expansion of the Universe, and then use the FP to study the mean evolution of the galaxies in the clusters.

The FP zero point differences between the intermediate redshift clusters and the Coma cluster can be interpreted as differences in the M/L ratios. With the FP coefficients from JFK96 the M/L ratios can be expressed as

$$\begin{aligned}\log M/L &= 0.49\log\sigma + 0.22\log r_e - \gamma/0.82 + cst \\ &= 0.24(2\log\sigma + \log r_e) - 0.02\log r_e \\ &\quad -\gamma/0.82 + cst\end{aligned} \tag{10}$$

(cf., JFK96), where γ is the FP zero point. Under the assumption that no merging or accretion takes place, the mass and therefore $(2\log\sigma + \log r_e)$ is constant. We can then derive the differences in the M/L ratios from the differences in the FP zero points, ignoring the small term $0.02\log r_e$. Fig.

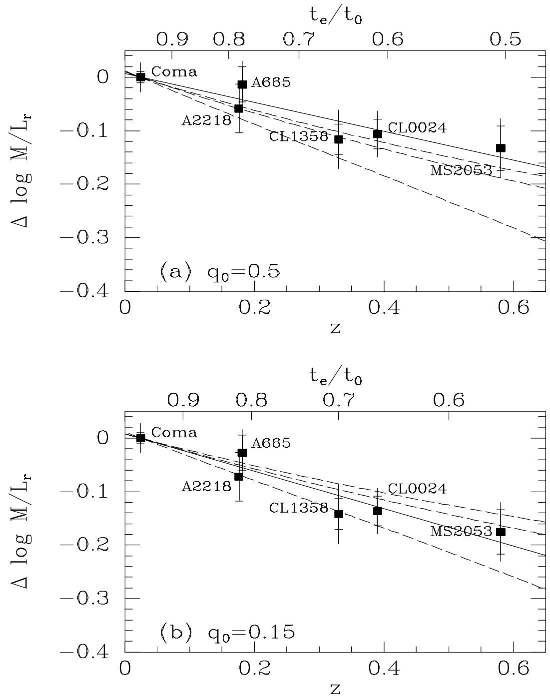

Figure 8. The evolution of the M/L ratio as function of the redshift of the clusters. The photometry has been calibrated to Gunn r in the rest frame of the clusters. The small and large error bars show the random and systematic uncertainties, respectively. These were derived as $\sigma(\log M/L) = \sigma(\log r_e)/0.82$. See Table 7 for values of $\sigma(\log r_e)$. (a) $q_o = 0.5$; (b) $q_o = 0.15$. The top axis on each panel shows the time of emission in units of the present age of the Universe. Solid lines – least squares fits to the data. Dashed lines – passive evolution with $z_{form} = \infty, 5$ and 1 (top to bottom).

8 shows the differences in the M/L ratios as a function of the redshifts.

The galaxies in A665 and A2218 have on average M/L ratios (11 ± 7)% smaller than the M/L ratios of the galaxies in the Coma cluster. Together with the previous data from van Dokkum & Franx (1996) and Kelson et al. (1997), this shows the gradual and slow evolution of the M/L ratio of the galaxies as a function of the redshift. A least squares fit to the all data shown on Fig. 8 gives $\Delta \log M/L_r = (-0.26 \pm 0.06)\Delta z$ for $q_o = 0.5$ and $\Delta \log M/L_r = (-0.34 \pm 0.06)\Delta z$ for $q_o = 0.15$. For the photometry calibrated to Johnson V we find $\Delta \log M/L_V = (-0.29 \pm 0.08)\Delta z$ and $\Delta \log M/L_V = (-0.37 \pm 0.08)\Delta z$ for $q_o = 0.5$ and 0.15, respectively. Our results in Johnson V are in agreement with the results by van Dokkum & Franx and Kelson et al.

The M/L ratio of a stellar population can be modeled as

$$M/L \propto t^{\kappa} \tag{11}$$

where t is the age of the stellar population (Tinsley 1980). The coefficient κ depends on the initial mass function (IMF) of the stars and on the passband. Based on the single burst stellar population models from Vazdekis et al. (1996), we find for photometry in Gunn r that $\kappa_r \approx 0.9 - 0.2x$ where x is the slope of the IMF. A Salpeter (1955) IMF has $x = 1.35$ (equivalent to $\kappa_r \approx 0.6$). For photometry in Johnson V, the expected evolution is nearly the same. The models from Vazdekis et al. give $\kappa_V \approx 0.95 - 0.2x$.

Equation (11) can be used to relate the change in the M/L ratio with redshift to the formation redshift, z_{form}, and the value of q_o. The dashed lines on Fig. 8 show the expected relations for $\kappa = 0.6$ and $z_{form} = \infty, 5$ and 1. Models with shallower IMFs make the slope of the expected relation steeper, while a model with steeper IMFs make the slope of the relation shallower.

For $q_o = 0.5$, the models with a Salpeter IMF and $z_{form} > 5$ are consistent with the data within 2σ. A formation redshift of $z_{form} = 2.4$ represents a 3σ deviation. Models with z_{form} smaller than 2.4 deviate more than 3σ from the fit to the data. If we assume $q_o = 0.15$ more models are consistent with the data. A model with a Salpeter IMF then implies $z_{form} \approx 2.5$. Models with z_{form} in the interval 1.7–6.5 are consistent with the data within 2σ. Models with $z_{form} < 1.4$ deviate more than 3σ from the fit to the data.

Because of the larger number of clusters analyzed here we are able to put stronger formal limits on the formation redshift, z_{form}, than done in previous studies (van Dokkum & Franx 1996; Kelson et al. 1997). However, the derived model constraints should only be taken as rough guidelines. The correct interpretation of the data is most likely rather more complicated than indicated here. The correct value of κ is not known. Further, the evolution of E and S0 galaxies cannot be viewed as a single burst event. The presence of younger stellar populations in the galaxies would imply stricter lower limits on z_{form}. The most fundamental assumption for the interpretation of the data is that the observed E and S0 galaxies in the intermediate redshift clusters in fact evolve into galaxies similar to the present day E and S0 galaxies. It is possible that our selection of E and S0 galaxies in the intermediate redshift clusters is biased to select already aged galaxies (see also Franx & van Dokkum 1996). In this case we are likely to underestimate the mean evolution measured from the FP when comparing to complete samples of galaxies in nearby clusters. Larger and more complete samples in intermediate redshift clusters are needed in order to address this problem in detail.

6 CONCLUSIONS

We have established the Fundamental Plane (FP) for the two rich clusters Abell 665 and Abell 2218, both at a redshift of 0.18. The photometric parameters were derived from ground-based observations obtained with the Nordic Optical Telescope, La Palma, and from HST observations. The photometry was calibrated to Gunn r in the rest frame of the clusters. Central velocity dispersions were measured for six galaxies in A665 and ten galaxies in A2218. The FPs for the two clusters were compared to the FP for nearby clusters derived by JFK96, and to the FP for the Coma cluster. The scatter around the FP for A665 and A2218 is similar to the scatter found for nearby clusters.

We have used the data for A665 and A2218 together with other recently available data for intermediate redshift clusters (van Dokkum & Franx 1996; Kelson et al. 1997) to test if the slope of the FP changes with redshift. The data for the clusters CL0024+16 (z=0.39), CL1358+62 (z=0.33) and MS2053-04 (z=0.58) were calibrated to Gunn r in the rest frame of the clusters. We find that the coefficient for the $\log \sigma$ term in the FP is significantly smaller for the intermediate redshift clusters than for the Coma cluster. The difference cannot be explained by the difference in the luminosity distribution of the Coma cluster sample and the samples in the intermediate redshift clusters. However, other types of selection effects, like a difference in the distribution of the combination $\log r_{\rm e} + 0.82 \log <I>_{\rm e}$, have not been ruled out. The smaller value of the coefficient implies that $M/L \propto M^{0.44} {r_{\rm e}}^{-0.17}$ for the intermediate redshift clusters, compared to $M/L \propto M^{0.24} {r_{\rm e}}^{-0.02}$ for nearby clusters (JFK96). This may indicate that the low mass galaxies in the clusters evolve faster than the more massive galaxies. We cannot distinguish if this is purely a difference in the luminosity evolution or if also dynamical evolution takes place. Alternatively, the velocity dispersion and not the mass could be the driving parameter. Direct fits to the M/L ratio as a function of the velocity dispersion give $M/L \propto \sigma^{0.66}$ for the Coma cluster and $M/L \propto \sigma^{1.49}$ for the intermediate redshift clusters.

The zero point offsets in the FP for the intermediate redshift clusters were used to investigate the average evolution of the M/L ratios of the galaxies. The M/L ratios of the galaxies in A665 and A2218 are on average $(11 \pm 7)\%$ smaller than the M/L ratios of the galaxies in the Coma cluster. From all the clusters we find that the M/L ratio changes with the redshift as $\Delta \log M/L_r = (-0.26 \pm 0.06) \Delta z$ (for $q_{\rm o} = 0.5$), equivalent to a change in the absolute magnitudes of $\Delta M_{\rm r_T} = (-0.65 \pm 0.15) \Delta z$. The slow evolution of the M/L ratios as a function of redshifts that we find is in general agreement with previous results by van Dokkum & Franx (1996), Kelson et al. (1997), Bender et al. (1998) and Pahre et al. (1999). The result can be used to constrain the formation redshift of the galaxies. The interpretation depends on the crucial assumption that the E and S0 galaxies observed in the intermediate redshift clusters evolve into galaxies similar to present day E and S0 galaxies (cf., Franx & van Dokkum 1996), and that the samples in the intermediate redshift clusters form a representative sample of all the galaxies that will end as present day E and S0 galaxies. For $q_{\rm o} = 0.5$, models with a single burst population, a Salpeter IMF and $z_{\rm form} > 5$ are consistent within 2σ with the observed evolution of the M/L ratios. Models with $z_{\rm form} < 2.4$ deviate more than 3σ from a least squares fit to the data. For $q_{\rm o} = 0.15$, we find $z_{\rm form} \approx 2.5$, while models with $z_{\rm form} < 1.4$ deviate more than 3σ from the fit to the data. The model constraints presented here are stronger than in previous studies due to the larger number of clusters included in the analysis.

Acknowledgements: The staff at NOT, KPNO and MMT are thanked for assistance during the observations. L. Davis is thanked for providing standard magnitudes for stars in M92. K. Kuijken and D. Kelson are thanked for making the template star observations available. Financial support from the Danish Board for Astronomical Research is acknowledged. Support for this research was provided by NASA through grant number HF-1016.01.91A to MF and grant number HF-01073.01.94A to IJ, both grants from the Space Telescope Science Institute, which is operated by the Association of Universities for Research in Astronomy, Inc., under NASA contract NAS5-26555. JH was supported in part by the Danish Natural Science Research Council.

REFERENCES

Bender R., Burstein D., Faber S. M., 1992, ApJ, 399, 462
Bender R., Saglia R. P., Ziegler B., Belloni P., Greggio L., Hopp U., Bruzual G., 1998, ApJ, 493, 529
Butcher H., Oemler A. Jr., Wells D. C., 1983, ApJS, 52, 183
Caldwell N., Rose J. A., Sharples R. M., Ellis R. S., Bower R. G., 1993, AJ, 106, 473
Christian C. A., Adams M., Barnes J. V., Butcher H., Hayes D. S., Mould J. R., Siegel M., 1985, PASP, 97, 363
Coleman G. D., Wu C.-C., Weedman D. W., 1980, ApJS, 43, 393
Couch W. J., Barger A. J., Smail I., Ellis R. S., Sharples R. M., 1998, ApJ, 497, 188
Davies R. L., Burstein D., Dressler A., Faber S. M., Lynden-Bell D., Terlevich R. J., Wegner G., 1987, ApJS, 64, 581
Davis L., 1994, private communication
Djorgovski S., Davis M., 1987, ApJ, 313, 59
Dressler A., 1987, ApJ, 317, 1
Dressler A., Lynden-Bell D., Burstein D., Davies R. L., Faber S. M., Terlevich R. J., Wegner G., 1987, ApJ, 313, 42
Dressler A., Oemler A. Jr., Butcher H., Gunn J. E., 1994a, ApJ, 430, 107
Dressler A., Oemler A. Jr., Sparks W. B., Lucas R. A., 1994b, ApJ, 435, L23
Dressler A., Oemler A. Jr., Couch W. J., Smail I., Ellis R. R., Barger A., Butcher H., Poggianti B. M., Sharples R. M., 1997, ApJ, 490, 577
Ellis R. S., Smail I., Dressler A., Couch W. J., Oemler A. Jr., Butcher H., Sharples R. M., 1997, ApJ, 483, 582
Faber S. M., Dressler A., Davies R. L., Burstein D., Lynden-Bell D., Terlevich R. J., Wegner G., 1987, in Faber S. M., eds, Nearly Normal Galaxies, New York, Springer-Verlag, p. 175
Faber S. M., Trager S. C., Gonzales J. J., Worthey G., 1995, in van der Kruit P. C., Gilmore G., eds, Stellar Populations, IAU coll. 164, Kluwer, Dordrecht, p. 249
Faber, S. M., Wegner, G., Burstein, D., Davies, R. L., Dressler, A., Lynden-Bell, D., Terlevich, R. J. 1989, ApJS, 69, 763
Franx M., 1993a, ApJ, 407, L5
Franx M., 1993b, PASP, 105, 1058
Franx M., van Dokkum P. G., 1996, in Bender R., Davies R., eds., Proc. IAU Symp. 171, New Light on Galaxy Evolution, Kluwer, Dordrecht, P. 233
Franx M., Illingworth G., Heckman T., 1989a, AJ, 98, 538
Franx M., Illingworth G., Heckman T., 1989b, ApJ, 344, 613
Frei Z., Gunn J. E., 1994, AJ, 108, 1476
Fukugita M., Shimasaku K., Ichikawa T., 1995, PASP, 107, 945
Hill R. J., et al., 1998, ApJ, 496, 648
Hjorth J., Madsen J., 1995, ApJ, 445, 55
Holtzman J., et al., 1995a, PASP, 107, 156
Holtzman J., Burrows C. J., Casertano S., Hester J., Trauger J. T., Watson A. M., Worthey G., 1995b, PASP, 107, 1065
Joner M. D., Taylor B. J., 1990, PASP, 102, 1004
Jørgensen I., 1999, MNRAS, in press (astro-ph/9902250)
Jørgensen I., 1994, PASP, 106, 967
Jørgensen I., Franx M., 1994, ApJ, 433, 553
Jørgensen I., Franx M., Kjærgaard P., 1992, A&AS, 95, 489
Jørgensen I., Franx M., Kjærgaard P., 1993, ApJ, 411, 34
Jørgensen I., Franx M., Kjærgaard P., 1995a, MNRAS, 273, 1097
Jørgensen I., Franx M., Kjærgaard P., 1995b, MNRAS, 276, 1341
Jørgensen I., Franx M., Kjærgaard P., 1996, MNRAS, 280, 167

Kelson D., van Dokkum P. G., Franx M., Illingworth G. D., Fabricant D., 1997, ApJ, 478, L13
Kneib J.-P., Mellier Y., Pelló R., Miralda-Escudé J., Le Borgne J.-F., Böhringer H., Picat J.-P., 1995, A&A, 303, 27
Krist J., Hook R., 1997, The Tiny Tim User's Manual, version 4.4, STScI, Baltimore
Landolt A. U., 1992, AJ, 104, 340
Le Borgne J. F., Pelló R., Sanahuja B., 1992, A&AS, 95, 87
Lilly S. J., Le Fevre O., Hammer F., Crampton D., 1996, ApJ, 460, L1
Lucey J. R., Guzmán R., Carter D., Terlevich R. J., 1991, MNRAS, 253, 584
Milvang-Jensen B., Jørgensen I., 1999, in preparation
Montgomery K. A., Marschall L. A., Janes K. A., 1993, AJ, 106, 181
Moore B., Katz N., Lake G., Dressler A., Oemler A. Jr., 1996, Nature, 379, 613
Oegerle W. R., Fitchett M. J., Hill J. M., Hintzen P., 1991, ApJ, 376, 46
Oemler A. Jr., Dressler A., Butcher H., 1997, ApJ, 474, 561
Pahre M., Djorgovski S. G., de Carvalho R. R., 1999, in Carral P., Cepa J., eds., Star Formation in Early Type Galaxies, ASP Conf. Series Vol. 163, Astron. Soc., Pac., San Fransisco, 17
Rakos K. D., Schombert J. M., 1995, ApJ, 439, 47
Salpeter E. E., 1955, ApJ, 121, 161
Schlegel D., Finkbeiner D., Davies M., 1998, ApJ 500, 525
Smith R. J., Lucey J. R., Hudson M. J., Steel J., 1997, MNRAS, 291, 461
Stetson P. B., Harris W. E., 1988, AJ, 96, 909
Tinsley B. M., 1980, Fundam. Cosmic Phys., 5, 287
Tully R. B., Fisher J. R., 1977, A&A, 54, 661
van Dokkum P. G., Franx M., 1996, MNRAS, 281, 985
van Dokkum P. G., Franx M., Kelson D. D., Illingworth G. D., 1998, ApJ 504, L17
Vazdekis A., Casuso E., Peletier R. F., Beckman J. E., 1996, ApJS, 106, 307
Vogt N. P., Forbes D. A., Phillips A. C., Gronwall C., Faber S. M., Illingworth G. D., Koo D. C., 1996, ApJ, 465, L15
Wegner G., Colless M., Saglia R. P., McMahan Jr. R. K., Davies R. L., Burstein D., Baggley G., 1998, MNRAS, in press (astro-ph/9811241)

APPENDIX A: THE PHOTOMETRY

A1 Basic reductions of ground-based images

The bias level and pattern turned out to depend on the CCD temperature, which in turn varied with ± 1.0K. Therefore, the bias was subtracted row-by-row based on the overscan region of the images. After this processing a few of the images showed row-to-row variations in the background of 1-1.5%. The level of these variations were determined directly from the images, and subtracted out with appropriate filtering to ensure the levels were not affected by signal from the objects. No correction for the dark current was performed. The dark current is less than $2e^-$ per hour.

The offset between the set exposure time and the actual exposure time for the iris shutter of the camera was determined from dome flats. The average shutter correction is $\Delta = 0.0826 \pm 0.0008$ sec.

The linearity of the CCD was tested from dome flats. No signs of non-linearity can be detected within the detection accuracy of 1.5%, for levels up to the software saturation limit.

Flat fields were constructed from twilight flat fields. Further, the low frequency variations over the fields were corrected for by using night time exposures of blank fields. Dust grains gave rise to flat field variations from night to night, and sometimes during the night. Night time exposures of blank fields were also used to correct for this effect. The pixel-to-pixel accuracy of the flat fields is 0.2-0.4% in areas not affected by the dust grains, and 0.8% in areas affected by the dust grains. The low frequency variations over the field and any residuals from the dust grains are below 0.5% after the flat field correction.

The I-band images of the two galaxy clusters were combined and cleaned for signal from cosmic-ray-events (CR) as follows. Geometrical transformations (shifts in x and y and a rotation) were used to transform all images of a field to a common reference image. The median sky level was subtracted from each image, and the relative intensity was determined from aperture photometry of objects brighter than $\approx 20\overset{\mathrm{m}}{.}5$ in the I-band. A median image was constructed, each image scaled according to the relative intensity. Each image was then compared to the median image and deviations larger than seven times the local noise were flagged as CRs. Mask images of the flagged pixels as well as other bad pixels due to the CCD were constructed. Finally, a mean image was derived, omitting the flagged pixels, and each individual image scaled according to the relative intensity of the image. To maintain the statistically properties of the mean image, the mean of the median sky levels was added to the final image. The masks were inspected visually to make sure no signal from objects got masked. Further, the cleaned mean image was compared with a mean image with no masking by means of aperture photometry of the objects in the field.

The magnitude zero points for the combined images were established by comparing aperture photometry from these images to aperture photometry derived from the individual images. Photometry was derived for 40-60 objects with I-band magnitudes brighter than $\approx 20\overset{\mathrm{m}}{.}5$. The consistency of the zero points is better than $0\overset{\mathrm{m}}{.}015$.

A2 Basic reduction of HST images

The HST/WFPC2 images were corrected for bias, dark-current and flat field corrected using the pipeline reduction supplied by Space Telescope Science Institute. The images were co-added and cleaned for cosmic-ray-events using the iterative method implemented in the Space Telescope Science Data Analysis Software (STSDAS) task "crrej". Where necessary, the individual images were first registered by applying small integer pixel shifts.

A3 Calibration to standard passbands

A3.1 Ground-based photometry

The NOT photometry was standard calibrated based on observations of stars in M67, M92, and the field SA101 taken during the nights of the galaxy observations. All nights during which galaxy observations were obtained were photometric. Aperture photometry was derived for 188 observations of a total of 35 stars. The observations have large variations in the seeing, and some of the exposures were taken with the telescope slightly defocused due to the brightness of the stars. The aperture radii for the photometry were typically

$4''.9$. Based on growth curves of bright stars in the fields the aperture magnitudes were corrected for the finite sizes of the apertures. The growth curves typically extended to $9''.5$, and the typical size of the correction is $-0^{\rm m}.04$. This correction ensures consistency between the defocused and focused observations, and between observations with large differences in the seeing. All observations in the I-band were obtained during night 1 and night 5. All observations in the V-band were obtained during night 2. The typical seeing for the standard star observations was FWHM=$0''.6-0''.7$, $1''.5-2''.5$ and $0''.7-1''.0$ for the nights 1, 2 and 5, respectively.

The 9-15 stars in M67 were used for determination of the atmospheric extinction. We find $k_I(\text{night1}) = 0.063 \pm 0.001$, $k_I(\text{night5}) = 0.124 \pm 0.001$, and $k_V(\text{night2}) = 0.165 \pm 0.004$. Further, observations from night 5 were offset to consistency with night 1 by subtraction of $0^{\rm m}.011$.

We have used standard magnitudes from Landolt (1992) (SA101) and Davis (1994) (M92). The magnitudes from Davis are consistent with Christian et al. (1985) and Stetson & Harris (1988) for the stars in common. The standard magnitudes from M67 are from Montgomery et al. (1993), Joner & Taylor (1990) and Jørgensen (1994), in this priority. The magnitudes from the three sources are consistent for the stars in common. We derived the following standard transformations

$$\begin{array}{ll} I_c = I_{\rm inst} + {\rm cst} & {\rm rms} = 0.021 \\ V = V_{\rm inst} + 0.0596(V-I)_{\rm inst} + {\rm cst} & {\rm rms} = 0.014 \end{array} \quad ({\rm A1})$$

The I magnitudes were calibrated to Cousins I_c. The transformation for I_c has no significant color term; if we include a $(V-I)$ term in the transformation we find a coefficient for this term of 0.001 ± 0.007. The photometry for the galaxies was corrected for the galactic extinction. For A665, the galactic extinction is $A_{\rm B} = 0.15$ equivalent to $A_{\rm I} = 0.07$ and $A_{\rm V} = 0.11$. A2218 has a galactic extinction in the B-band of $A_{\rm B} = 0.10$, equivalent to $A_{\rm I} = 0.05$ and $A_{\rm V} = 0.08$. The galactic extinctions were derived from the reddening maps published by Schlegel, Finkbeiner & Davis (1998).

A3.2 Photometry from HST observations

The photometry from the HST images was calibrated using the transformations given by Holtzman et al. (1995b). For F814W we use the transformation based on observations, while for F606W and F702W we use the synthetic transformations. We define instrumental magnitudes as

$$m_{\rm inst} = -2.5\log({\rm DN}/t_{\rm exp}) + {\rm ZP} + 2.5\log {\rm GR}_i + \Delta m + 0.05 \quad ({\rm A2})$$

"DN" is the number of counts, "ZP" are the zero points given by Holtzman et al. (1995b) for the relevant transformation (see equations [A4] and [A5]). We use ${\rm GR}_2 = 2.003$, ${\rm GR}_3 = 2.006$ and ${\rm GR}_4 = 1.955$. The term 0.05 is added as a correction for the difference between "short" and "long" exposures (Hill et al. 1998). The aperture corrections Δm were estimated from data for the encircled energy given by Holtzman et al. (1995a). We use $\Delta m_{814} = 0.0983$, $\Delta m_{702} = 0.1087$, and $\Delta m_{606} = 0.1138$. The instrumental magnitudes in the three filters are then given by

$$\begin{array}{lcl} m_{814} & = & -2.5\log({\rm DN}/t_{\rm exp}) + 20.987 + 2.5\log {\rm GR}_i \\ m_{702} & = & -2.5\log({\rm DN}/t_{\rm exp}) + 21.670 + 2.5\log {\rm GR}_i \\ m_{606} & = & -2.5\log({\rm DN}/t_{\rm exp}) + 22.257 + 2.5\log {\rm GR}_i \end{array} \quad ({\rm A3})$$

The photometry for galaxies in A665 was calibrated using the transformations for I_c and V and colors based on HST data. We use the following transformations

$$\begin{array}{lcl} I_c & = & m_{814} - 0.062(V-I_c) + 0.025(V-I_c)^2 \\ V & = & m_{606} + 0.254(V-I_c) + 0.012(V-I_c)^2 \end{array} \quad ({\rm A4})$$

The I_c transformation is for the in-flight system based on stars bluer than the typical colors of the observed galaxies, $(V-I_c) = 1.5$. However, for $(V-I_c) = 1.5$ the transformation agrees within $0^{\rm m}.005$ with the synthetic transformation.

A2218 was observed in the F702W filter, only. We have calibrated this photometry to I_c using the transformation for R_c given by Holtzman et al. (1995b) and the relation $(V-R_c) = 0.52(V-I_c)$, which we derived from standard star magnitudes for stars with $(V-I_c)$ in the interval 1–2 (Landolt 1992). The coefficient is in agreement with colors of E and S0 galaxies at $z = 0.2$ (e.g., Fukugita, Shimasaku & Ichikawa 1995; Frei & Gunn 1994). This gives the transformation

$$I_c = m_{702} - 0.227(V-I_c) - 0.021(V-I_c)^2 \quad ({\rm A5})$$

We used colors from the ground-based photometry in order to calibrate the HST observations of A2218. Finally, the photometry was corrected for the galactic extinction.

A4 Photometric parameters

Tables A1 and A2 give the effective parameters and colors of all galaxies in the two clusters brighter than $m_{\rm T} = 19^{\rm m}$ in I_c and within the fields covered by the NOT observations. Five of the galaxies in A665 were also observed by Oegerle et al. (1991). The cross-references are as follows, with our galaxy number given first. 1032 = 218, 1150 = 201, 1168 = 224, 2105 = 225 and 2122 = 227.

A5 Comparison of ground-based and HST photometry

The ground-based photometry and the HST photometry were compared by means of aperture magnitudes. In order to limit the effect of the different spatial resolution and the choice of the aperture size we convolved the HST images to approximately the same resolution as the ground-based images. Aperture magnitudes for the galaxies were then derived within apertures of with radii of 3 arcsec. The magnitudes were standard calibrated as described in Sections A3.1 and A3.2. Fig. A1 show the comparison of the aperture magnitudes. We find the mean differences to be $I_c({\rm NOT}) - I_c({\rm HST}) = 0.066 \pm 0.007$ and 0.017 ± 0.010 for A665 and A2218, respectively. Galaxies with aperture magnitude fainter than $19^{\rm m}$ were excluded from this comparison in order to limit the errors introduced by uncertainty in the sky subtraction.

The effective parameters derived from the NOT images and the HST images were compared, see Fig. A2 and Table A3. Only the galaxies with total magnitudes brighter than $19^{\rm m}$ in the I-band were included in this comparison, a total of 56 galaxies. For the fainter galaxies the individual parameters ($\log r_{\rm e}$, $\langle\mu\rangle_{\rm e}$ and $m_{\rm T}$) become highly uncertain due to the small size of the galaxies compared to the FWHM of the PSF for the ground-based data, and due to rather low signal-to-noise for these faint galaxies in the HST observations of

TABLE A1

Photometric parameters, Abell 665

Galaxy	R.A. (J2000)	Dec. (J2000)	Field	NOT log r_e [arcsec]	NOT $\langle\mu\rangle_e$ (I_c)	NOT χ^2/N_{pix}	NOT $(V-I_c)$	HST log r_e [arcsec]	HST $\langle\mu\rangle_e$ (F606W)	HST $\langle\mu\rangle_e$ (V)	HST χ^2/N_{pix} (F606W)	HST log r_e [arcsec]	HST $\langle\mu\rangle_e$ (F814W)	HST $\langle\mu\rangle_e$ (I_c)	HST χ^2/N_{pix} (F814W)	HST $(V-I_c)$
1022	8:31:00.34	65:49:00.2	1	-0.248	19.30	1.8	1.49	-0.172	20.71	21.01	2.3	-0.172	19.63	19.59	1.9	1.46
1032	8:31:10.37	65:49:17.3	1	-0.010	19.15	3.4	1.55	0.063	20.56	20.88	4.4	0.037	19.36	19.32	3.5	1.52
1035	8:30:55.99	65:49:12.4	1	0.049	19.54	2.0	1.53	0.121	20.93	21.24	1.6	0.088	19.71	19.67	1.4	1.50
1040	8:31:06.97	65:49:20.2	1	0.091	19.92	1.2	1.52	0.170	21.32	21.62	1.8	0.144	20.14	20.10	2.1	1.49
1044	8:31:07.66	65:49:25.0	1	-0.257	18.84	1.6	1.53	...	...	...	...	...	...	...	...	...
1046	8:31:11.34	65:49:28.5	1	-0.080	19.47	1.5	1.54	0.035	21.03	21.33	1.9	0.027	19.92	19.88	1.6	1.49
1060	8:31:07.73	65:49:36.4	1	0.243	21.55	1.7	1.44	0.221	22.56	22.86	1.8	0.209	21.47	21.43	1.6	1.45
1067	8:31:06.35	65:49:39.2	1	-0.122	20.37	2.1	1.45	0.092	22.25	22.55	2.6	0.111	21.25	21.21	2.2	1.48
1069	8:31:02.03	65:49:37.4	1	0.109	20.41	1.5	1.51	0.081	21.44	21.74	1.5	0.072	20.32	20.27	1.4	1.48
1084	8:30:55.96	65:49:47.4	1	-0.226	18.24	3.0	1.56	...	...	...	...	...	...	...	...	...
1114	8:30:55.20	65:50:06.7	1	-0.154	18.86	1.7	1.53	-0.109	20.15	20.46	1.5	-0.034	19.37	19.33	1.2	1.47
1134	8:30:59.22	65:50:21.6	1	-0.302	19.01	14.9	1.38	...	...	...	...	...	...	...	...	...
1138	8:30:58.71	65:50:23.7	1	0.289	20.22	15.7	1.53	...	...	...	...	...	...	...	...	...
1150	8:30:57.36	65:50:30.4	1	1.012	21.82	2.9	1.54	1.070	23.15	23.47	4.4	1.056	22.01	21.97	5.2	1.53
1161	8:31:05.41	65:50:44.1	1	-0.249	19.59	1.8	1.47	-0.188	20.94	21.24	1.8	-0.190	19.86	19.82	1.3	1.47
1164	8:31:00.86	65:50:43.5	1	-0.422	18.40	3.7	1.54	-0.166	20.56	20.88	2.9	-0.170	19.43	19.39	2.2	1.52
1166	8:30:55.32	65:50:41.5	1	-0.262	18.75	3.1	1.54	-0.317	19.68	19.98	3.6	-0.223	18.96	18.92	2.1	1.47
1167	8:30:58.68	65:50:43.3	1	-0.399	18.44	3.9	1.56	-0.117	20.62	20.94	4.1	-0.112	19.51	19.47	3.3	1.54
1168	8:31:03.25	65:50:48.1	1	0.333	19.78	2.1	1.54	0.382	21.09	21.40	2.0	0.376	19.97	19.93	1.3	1.52
1191	8:30:59.37	65:50:58.0	1	0.070	20.87	4.3	1.34	0.334	22.82	23.09	3.5	0.358	21.90	21.85	2.1	1.37
1193	8:30:56.51	65:50:58.5	1	0.015	20.77	1.3	1.44	0.157	22.31	22.60	1.8	0.159	21.25	21.21	1.2	1.45
1196	8:31:05.16	65:51:04.6	1	-0.352	17.73	9.0	1.51	-0.125	19.77	20.07	10.5	-0.149	18.62	18.58	7.9	1.47
1202	8:30:55.79	65:51:03.2	1	-0.256	19.43	1.5	1.52	-0.118	21.04	21.34	3.3	-0.107	20.00	19.96	4.6	1.49
2007	8:30:55.59	65:49:01.8	2	-0.187	18.70	1.9	1.57	-0.182	19.83	20.14	8.6	-0.191	18.71	18.67	8.0	1.49
2023	8:30:54.48	65:49:24.9	2	-0.252	19.47	1.3	1.52	-0.209	20.74	21.05	2.3	-0.195	19.70	19.66	1.9	1.49
2029	8:30:52.46	65:49:26.6	2	-0.344	18.61	1.6	1.56	...	...	...	...	...	...	...	...	...
2063	8:30:48.79	65:50:01.3	2	0.264	20.68	5.2	1.51	0.112	21.25	21.55	2.1	0.150	20.32	20.27	1.4	1.47
2081	8:30:54.45	65:50:23.6	2	-0.404	18.97	1.7	1.53	-0.449	19.92	20.22	1.1	-0.339	19.28	19.24	0.9	1.46
2092	8:30:43.11	65:50:25.6	2	-0.194	18.94	2.2	1.52	...	...	...	...	...	...	...	...	...
2096	8:30:40.03	65:50:26.3	2	0.494	21.79	5.6	1.20	...	...	...	...	...	...	...	...	...
2105	8:30:42.21	65:50:35.7	2	0.876	22.09	29.7	1.20	1.130	23.73	23.96	29.3	1.003	22.46	22.42	18.5	1.24
2108	8:30:39.23	65:50:36.1	2	-0.205	19.48	1.5	1.53	...	...	...	...	...	...	...	...	...
2111	8:30:53.35	65:50:43.5	2	-0.170	18.56	6.7	1.62	-0.058	20.13	20.44	4.0	-0.011	19.21	19.17	4.1	1.51
2122	8:30:43.39	65:50:44.8	2	0.566	21.71	20.1	1.11	0.543	22.48	22.69	22.9	0.594	21.85	21.80	12.3	1.12
2127	8:30:41.37	65:50:47.1	2	0.475	22.32	2.8	0.96	0.560	23.28	23.41	3.5	0.597	22.77	22.73	2.3	0.87
2144	8:30:50.19	65:51:07.5	2	-0.189	18.83	1.6	1.52	-0.192	19.92	20.20	2.2	-0.096	19.26	19.22	1.6	1.41
2159	8:30:53.69	65:51:23.7	2	-0.049	19.29	2.7	1.39	...	...	...	...	...	...	...	...	...

Note.— Galaxy identifications – this paper. Field – the NOT field that contains the galaxy, see Table 3 for seeing values. $\langle\mu\rangle_e(I_c)$, $\langle\mu\rangle_e(V)$ and $(V-I_c)$ for both the NOT and the HST data are standard calibrated to the Johnson-Kron-Cousins photometric system and corrected for galactic extinction. $\langle\mu\rangle_e$ (F814W) and $\langle\mu\rangle_e$ (F606W) are the instrumental magnitudes in F814W and F606W, respectively, see Eq. (A3). The formal fitting uncertainties are typically as follows. log r_e: ±0.006 for NOT data, ±0.002 for HST data. $\langle\mu\rangle_e$: ±0.02 for NOT data, ±0.007 for HST data. The typical (random) uncertainty on the $(V-I_c)$ is 0.01. The goodness-of-fit is given as χ^2/N_{pix}, where N_{pix} is the number of pixels within the fitting radius. $\chi^2=\sum(n_i-n_{i,model})^2/\sigma_i^2$, with the sum over all the pixels within the fitting radius. n_i is the signal in pixel i, $n_{i,model}$ is the model value in the pixel, and σ_i^2 the noise (photon- and read-out-noise) in the pixel. All the galaxies have been fitted with $r^{1/4}$ models.

TABLE A2

Photometric parameters, Abell 2218

Galaxy	R.A. (J2000)	Dec. (J2000)	NOT Field	NOT $\log r_e$ [arcsec]	NOT $<\mu>_e$ (I_c)	NOT χ^2/N_{pix}	NOT $(V-I_c)$	HST $\log r_e$ [arcsec]	HST $<\mu>_e$ (F702W)	HST $<\mu>_e$ (I_c)	HST χ^2/N_{pix}
L106	16:36:04.77	66:13:41.1	2	-0.381	18.48	1.3	...	...	...	...	...
L112	16:36:04.31	66:13:27.4	2	-0.163	19.52	2.8	1.47	-0.169	19.99	19.57	7.7
L113	16:36:04.17	66:13:23.9	2	-0.148	18.27	2.8	1.61	-0.017	19.24	18.77	7.4
L114	16:36:04.13	66:12:10.8	1	-0.159	19.49	1.7	1.50	...	...	...	...
L118	16:36:03.95	66:11:39.2	1	0.051	19.20	5.5	1.62	0.097	19.76	19.30	3.1
L119	16:36:03.67	66:13:32.5	2	0.010	19.74	4.9	1.46	...	...	...	...
L143	16:36:02.54	66:13:30.8	2	0.007	20.58	2.1	1.41	0.009	21.07	20.66	1.0
L148	16:36:02.23	66:11:51.7	1	-0.075	18.53	3.1	1.59	0.067	19.49	19.03	6.4
L149	16:36:02.15	66:12:33.3	1	0.190	19.55	2.3	1.55	...	...	...	...
L181	16:36:00.49	66:12:05.9	1	-0.155	20.02	1.8	1.38	-0.292	19.91	19.52	2.3
L185	16:36:00.35	66:12:19.5	1	0.095	21.46	1.3	1.29	...	...	...	...
L187	16:36:00.26	66:12:42.9	1	-0.353	18.24	1.7	1.55	...	...	...	...
L196	16:35:59.33	66:12:05.4	1	0.339	20.43	1.8	1.55	0.380	21.00	20.55	1.2
L198	16:35:59.31	66:12:52.3	1	-0.061	19.14	2.0	1.55	-0.143	19.25	18.81	1.9
L221	16:35:58.29	66:13:20.1	2	-0.123	19.73	1.5	1.61	-0.101	20.30	19.83	0.7
L232	16:35:57.35	66:12:14.5	1	-0.274	18.46	2.0	1.53	-0.322	18.70	18.26	4.6
L244	16:35:56.74	66:11:54.4	1	0.934	22.01	2.0	1.53	0.930	22.46	22.02	1.4
L246	16:35:56.66	66:12:39.9	1	-0.062	19.71	1.8	1.41	...	...	...	...
L259	16:35:56.25	66:11:49.9	1	-0.156	18.81	2.8	1.49	-0.170	19.18	18.75	3.1
L268	16:35:56.07	66:12:23.4	1	-0.072	20.62	1.4	1.24	0.121	21.66	21.30	3.9
L291	16:35:54.84	66:12:16.9	1	-0.033	20.42	1.7	1.35	0.150	21.45	21.07	2.7
L302	16:35:54.38	66:13:03.9	1	-0.403	18.80	1.8	1.52	-0.347	19.43	19.00	0.7
L319	16:35:53.33	66:12:31.3	1	0.405	22.27	2.1	1.47	...	...	...	...
L320	16:35:53.31	66:12:37.3	1	0.196	20.80	2.8	1.42	0.218	21.25	20.84	3.5
L341	16:35:51.80	66:12:33.1	1	-0.124	18.27	2.6	1.56	-0.116	18.71	18.26	4.1
L348	16:35:51.42	66:13:10.9	1	0.002	19.53	1.8	1.56	0.006	20.00	19.55	5.1
L360	16:35:50.73	66:12:19.2	1	-0.067	19.21	4.5	1.49	-0.065	19.65	19.22	8.5
L364	16:35:50.56	66:12:00.7	1	-0.221	19.63	1.5	1.49	-0.117	20.41	19.98	1.8
L371	16:35:50.18	66:12:18.3	1	-0.115	20.00	4.6	1.47	...	...	...	...
L373	16:35:49.94	66:12:22.6	1	0.153	19.44	4.9	1.54	0.008	19.35	18.91	10.8
L378	16:35:49.80	66:11:43.7	1	0.138	20.61	1.4	1.50	0.054	20.73	20.30	1.0
L385	16:35:49.41	66:12:35.0	1	-0.049	19.13	3.3	1.46	-0.215	18.93	18.51	6.5
L391	16:35:49.20	66:12:43.5	1	1.403	23.07	3.6	1.48	1.412	23.68	23.25	21.0
L395	16:35:49.00	66:12:59.7	1	-0.104	19.22	2.4	1.29	...	...	...	...
L404	16:35:48.75	66:12:08.5	1	0.008	20.75	1.3	1.43	-0.194	20.46	20.05	1.7
L421	16:35:47.55	66:12:41.4	1	-0.134	18.84	3.4	1.51	0.020	19.86	19.42	7.8
L430	16:35:47.22	66:13:14.8	2	-0.033	19.06	1.4	1.62	-0.061	19.42	18.95	1.0
L436	16:35:46.79	66:12:21.7	1	-0.086	19.26	1.9	1.50	-0.210	19.23	18.80	3.6
L442	16:35:47.53	66:12:31.2	1	-0.215	18.88	2.2	1.53	-0.275	19.07	18.63	5.5
L446	16:35:46.30	66:12:50.6	1	-0.025	19.57	1.7	1.49	-0.212	19.30	18.87	5.7
L448	16:35:45.95	66:12:31.7	1	-0.377	18.88	1.4	1.49	-0.527	18.74	18.32	2.6
L457	16:35:45.56	66:11:46.8	1	-0.444	18.56	1.6	1.52	...	...	...	...
L482	16:35:44.10	66:13:19.0	2	0.036	18.77	2.2	1.62	...	...	...	...
L484	16:35:43.89	66:11:54.6	1	0.236	21.33	2.4	1.39	...	...	...	...
L535	16:35:41.23	66:13:45.7	2	0.238	19.63	1.9	1.63	...	...	...	...
L542	16:35:40.84	66:12:35.5	1	-0.219	19.85	1.5	1.50	...	...	...	...
L553	16:35:40.05	66:12:55.1	1	-0.313	18.87	2.5	1.58	...	...	...	...
L554	16:35:39.99	66:11:39.9	1	-0.408	18.52	2.3	1.38	...	...	...	...
L589	16:35:37.13	66:12:57.3	1	-0.069	19.30	2.3	1.63	...	...	...	...
J1191	16:35:40.25	66:13:53.5	2	-0.255	18.86	1.8	1.56	...	...	...	...
BOW06	16:35:47.31	66:14:43.1	2	0.138	19.03	2.3	1.59	...	...	...	...
BOW25	16:35:54.64	66:13:59.0	2	0.294	20.18	2.0	1.54	...	...	...	...
BOW44	16:35:57.23	66:14:20.1	2	-0.195	18.52	1.7	1.67	...	...	...	...
BOW67	16:35:55.24	66:14:11.8	2	-0.051	19.39	1.9	1.64	...	...	...	...
BOW75	16:35:37.75	66:13:59.8	2	-0.027	19.72	2.7	1.61	...	...	...	...
BOW81	16:36:01.57	66:14:56.0	2	-0.137	19.27	1.4	1.60	...	...	...	...
BOW83	16:35:39.09	66:14:16.9	2	-0.085	19.94	4.6	0.95	...	...	...	...
BOW91	16:35:48.91	66:14:27.7	2	0.123	20.55	1.7	1.80	...	...	...	...
BOW97	16:35:39.97	66:14:46.9	2	0.046	20.29	1.8	1.88	...	...	...	...
BOW107	16:35:44.60	66:14:23.0	2	0.037	20.62	1.8	1.51	...	...	...	...
BOW116	16:35:42.35	66:14:12.2	2	-0.136	19.72	1.7	1.60	...	...	...	...

Note.— Galaxy identifications - Le Borgne et al. (1992) (L numbers), Butcher et al. (1983) (BOW numbers), this paper (J number). Field – the NOT field that contains the galaxy, see Table 3 for seeing values. $<\mu>_e(I_c)$ and $(V-I_c)$ for both the NOT and the HST data are standard calibrated to the Johnson-Kron-Cousins photometric system and corrected for galactic extinction. $<\mu>_e$ (F702W) is the instrumental magnitude in F702W, see Eq. (A3). The formal fitting uncertainties are typically as follows. $\log r_e$: ±0.006 for NOT data, ±0.002 for HST data. $<\mu>_e$: ±0.02 for NOT data, ±0.004 for HST data. The typical (random) uncertainty on the $(V-I_c)$ is 0.01. The goodness-of-fit is given as χ^2/N_{pix}, where N_{pix} is the number of pixels within the fitting radius. $\chi^2 = \sum (n_i - n_{i,\rm model})^2/\sigma_i^2$, with the sum over all the pixels within the fitting radius. n_i is the signal in pixel i, $n_{i,\rm model}$ is the model value in the pixel, and σ_i^2 the noise (photon- and read-out-noise) in the pixel. The galaxies L114, L395, BOW83 and BOW97 have been fitted with exponential disk models, all other galaxies have been fitted with $r^{1/4}$ models.

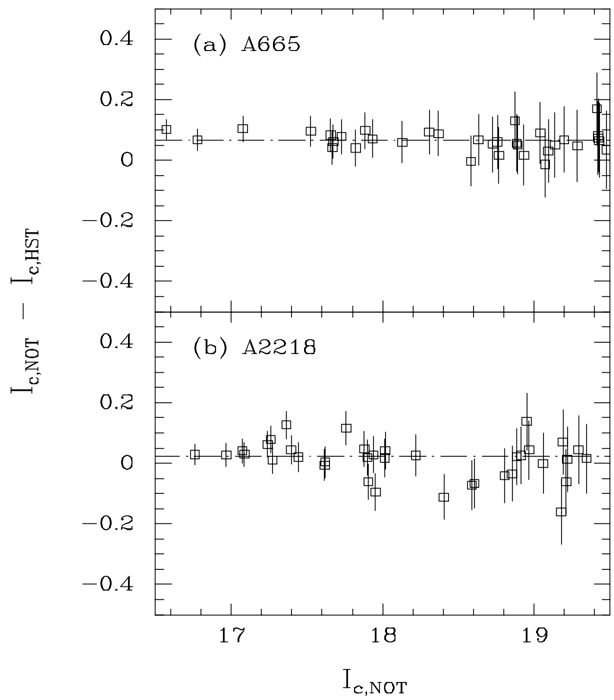

Figure A1. Comparison of aperture magnitudes. An aperture with radius 3 arcsec was used.

Table A3. Comparison of effective parameters

Parameter	mean difference	rms
$\log r_{\rm e}$	-0.033 ± 0.015	0.11
$<\mu>_{\rm e}$	-0.119 ± 0.053	0.41
$m_{\rm T}$	0.044 ± 0.021	0.16
FP[a]	0.006 ± 0.003	0.026

Notes. [a] the combination $\log r_{\rm e} - 0.328<\mu>_{\rm e}$. The differences are calculated as "NOT"–"HST". Only galaxies with total magnitudes brighter than $19^{\rm m}$ were included in the comparisons. The two clusters are combined in this table, and the HST photometry has been offset to consistency with the ground-based photometry, see text.

A665. The combination "FP"$=\log r_{\rm e} - 0.328<\mu>_{\rm e}$, which enters the FP, was also compared. This combination is well determined even for the fainter galaxies, but since none of the galaxies for which we have spectroscopy are fainter than $19^{\rm m}$ we restrict the comparisons to galaxies brighter than this limit. The rms scatter for the comparison of the combination "FP" is similar to typical values for comparisons of data for nearby clusters (e.g., Jørgensen et al. 1995a). If the uncertainty is equally distributed on two data sets, the typical uncertainty on the combination "FP" is 0.018. The small mean difference in the combination "FP" between the NOT data and the HST data is equivalent to a difference in the FP zero point of only 1.4%. The comparisons of the parameters $\log r_{\rm e}$, $<\mu>_{\rm e}$ and $m_{\rm T}$ have slightly larger scatter than usually found for comparisons between effective parameters for nearby galaxies derived by different authors.

The errors on $\log r_{\rm e}$ and $<\mu>_{\rm e}$ are highly correlated (e.g., Jørgensen et al. 1995a). We use this fact to provide

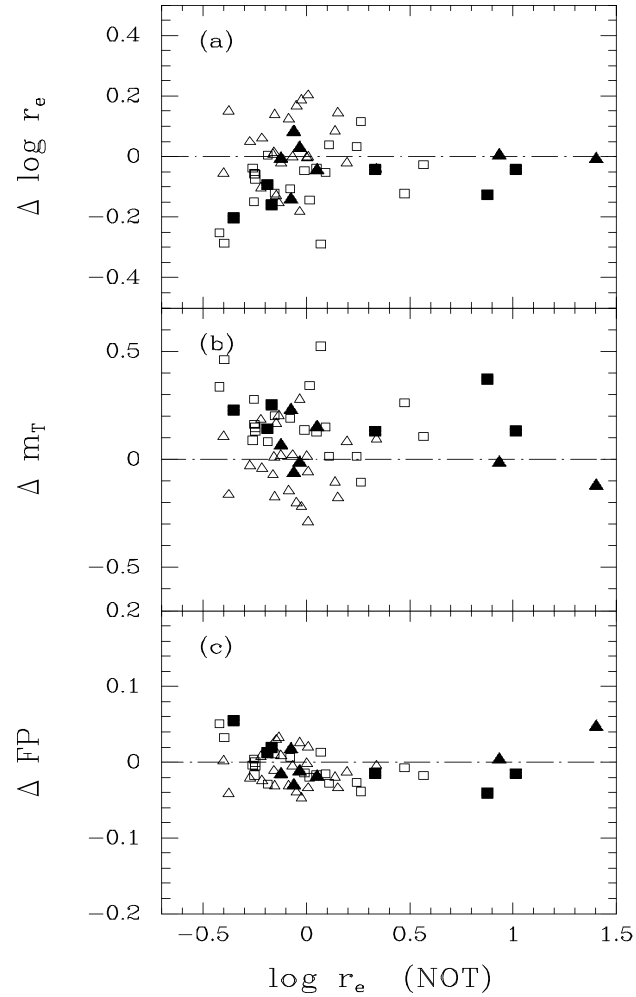

Figure A2. Comparison of effective parameters in the I-band. Boxes – A665; triangles – A2218. Solid symbols – galaxies for which we have spectroscopy. The differences are calculated as "NOT"–"HST". The formal errors derived from the fitting are of the size of the points. "FP" is the combination $\log r_{\rm e} - 0.328<\mu>_{\rm e}$ which enters the FP. Only galaxies with total magnitudes brighter than $19^{\rm m}$ are shown. The HST photometry shown on the figure has *not* been offset to consistency with the ground-based photometry.

another check of the magnitude zero points of the HST photometry. Fig. A3 shows the difference in $\log r_{\rm e}$ versus the difference in $<\mu>_{\rm e}$. The differences were calculated as "NOT"-"HST". The dashed lines on the panels show least squares fits to the data. If the zero point for the HST photometry was in perfect agreement with the ground-based zero point, then the dashed lines would go through (0,0). The offset in $\Delta<\mu>_{\rm e}$ is equal to the difference in the zero points. We find $I_c({\rm NOT}) - I_c({\rm HST}) = 0.063 \pm 0.011$ and 0.015 ± 0.008 for A665 and A2218, respectively. This is in agreement with the determinations of the zero point differences based on aperture magnitudes.

Offsets of a few hundredths of a magnitude are common between HST photometry and ground-based photometry (e.g., Ellis et al. 1997; Hill et al. 1998). The offset we

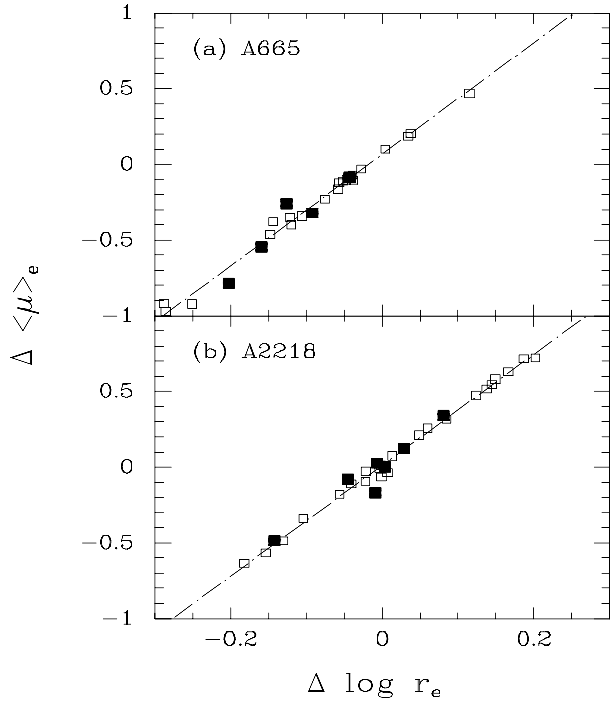

Figure A3. The difference in $\log r_e$ versus the difference in $<\mu>_e$. The differences are calculated as "NOT"-"HST". Only galaxies with total magnitudes brighter than 19^m are shown. Solid symbols – galaxies for which we have spectroscopy. The dashed lines show least squares fits to the data. The offset in $\Delta<\mu>_e$ can be used to derive the offset between the HST photometry and the ground-based photometry, see text.

find for the A665 photometry is slightly larger than expected. However, in order to ensure the consistency of the data for A665 and A2218 we have chosen to calibrate the HST photometry to the ground-based I_c. We have applied the following offsets: $I_c = I_c(\mathrm{HST}) + 0.065$ for A665 and $I_c = I_c(\mathrm{HST}) + 0.016$ for A2218.

We have no reliable way of checking the zero point for the V magnitudes based on the HST data, because of the poor seeing of our ground-based V-images. We have therefore not applied any zero point correction to the colors $(V - I_c)$ derived from the HST data.

APPENDIX B: SPECTROSCOPY

The spectroscopic observations were made through multi-slit masks. One field was observed in each cluster. The final spectra are shown in Figs. B1 and B2. The reductions of the A2218 spectra are described in the following. The methods for the reductions of the A665 spectra were very similar. We refer to Franx (1993ab) for additional information regarding the A665 spectra.

B1 A2218

The spectra were corrected for the bias and the dark by standard methods. The bias subtraction was based on the level in the overscan region as well as individual bias frames.

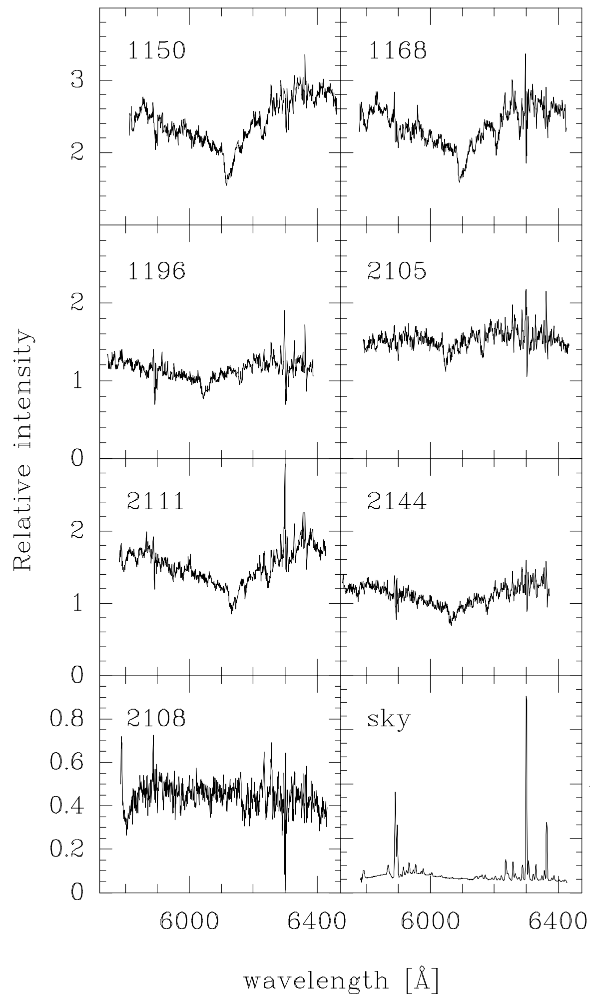

Figure B1. Spectra of the observed galaxies in A665. The spectra are not flux calibrated.

The flat fields show strong variations in the fringing depending on the zenith distance of the telescope due to the flexure of the instrument Therefore, flat fields obtained in day time did not give sufficiently good flat field correction. Instead we use flat fields obtained during the night. These flat fields were obtained with the internal quartz lamp in the instrument. Two flat fields bracket each science exposure. The flat fields obtained in day time were combined in the sets they were taken cleaned for cosmic-ray-events (CR). Then all the flat fields were normalized by fitting a high order spline in the direction of the dispersion. In order to clean the night time flat fields for CRs they were each compared to the the day time flat field, which best resembled night time flat field. The final flat fields were derived as the average of the two flat fields, which bracket the science exposure. The typical pixel-to-pixel noise in the final flat fields was 0.6%. Areas of the flat fields that had a pixel-to-pixel noise larger than 1.5% were set to one, and no flat field correction was performed. This also ensures that no artificial variations are introduced at the edges of the slit-lets.

The individual exposures of A2218 were cleaned for CRs as follows. First, the median image was derived. Then difference between each individual image and the median image was calculated. This image naturally has strong residuals from the sky lines and the galaxies. The residuals from the galaxies were fitted with a smooth function in the direction of the dispersion, and the fit was subtracted. The residuals from the sky lines were fitted with a constant across each slit-let, and the fit was subtracted. The resulting difference image contains noise and signal from CRs, plus some residuals from the strongest sky lines. Pixels for which the deviations were below 7 times the local noise or which had residuals from the sky lines were set to zero. This resulted in a mask image for each of the science exposures. The mask image was subtracted from its corresponding science exposure. The net-effect is that pixels affected by the CRs get substituted with the median value, variations due to the shifts of the galaxy spectra and the sky lines taken into account.

The spectra were corrected for the slit function based on sky flat fields. The derived slit function was shifted up to 0.4 pixel in the spatial direction in order to take into account the shifts in the slit-lets due to the flexure.

The wavelength calibration was done for each slit-let individually. The main wavelength calibration was established from high signal-to-noise He-Ne-Ar lamp spectra taken in day time. The dispersion solution was then shifted slightly based on He-Ne-Ar lamp spectra taken immediately before and after each science exposure. The typical rms of the wavelength calibration is 0.18Å.

The spectra were corrected for the S-distortion by tracing the position of the spectrum of the BCG. Because the signal in the individual exposures is too low to establish the S-distortion for the fainter galaxies the same S-distortion was used to correct all the galaxies. After the correction was applied, we verified that the same correction could be use for all the galaxies by deriving the differences between the mean center of the the spectra in the wavelength intervals 5295–5445Å and 6040–6130Å. The BCG has a difference of 0.02 pixels, while the rest of the galaxies show differences of less than 0.2 pixels. The aperture used for the velocity dispersion measurements is 5 pixels. We therefore conclude that the adopted correction for the S-distortion does not affect the velocity dispersion measurements.

The wavelength calibration and the correction for the S-distortion were applied simultaneously resulting in individual science exposures that are all on the same wavelength scale and with the galaxies centered on the same pixels. The spectra were sampled on a logarithmic wavelength scale. The individual images were then averaged with scaling according to their exposure time. The individual expsure times were 11×1h and one exposure of 48 minutes. The average image was at this stage cut into sub-images, each sub-image contains the spectrum from one slit-let. The sub-images are then treated as individual long-slit spectra.

The sky background was subtracted from each sub-image based on the outer $3\farcs5$-$10\farcs35$. When possible the sky spectra were extracted from both sides of the galaxy spectra. In some cases residuals were left from the stronger sky lines. The sky subtraction of these lines was improved by fitting a linear function to the residuals in the spatial direction, and then subtracting the fit. The residuals from the sky line at 5577Å were interpolated across.

The spectra were calibrated to a relative flux scale based on exposures of the flux standard star HD192281. The flux calibrated spectra are in this paper used for display purposes only. The determination of the velocity dispersions does not depend on the flux calibration.

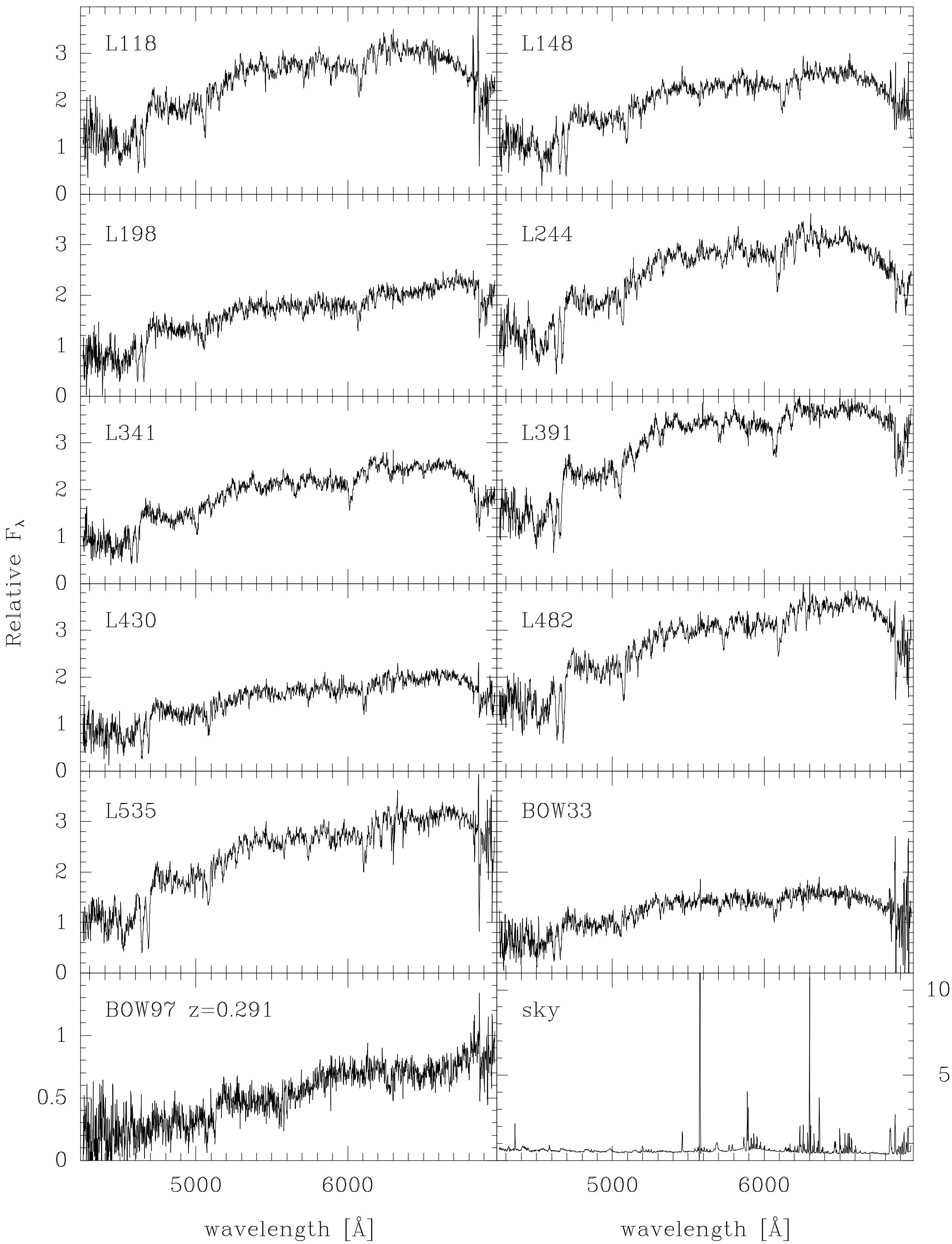

Figure B2. Spectra of the observed galaxies in A2218. The spectra are calibrated to a relative flux scale. The panels are labeled with galaxy numbers from Le Borgne et al. (1992) or Butcher et al. (1983). BOW97 is a background galaxy at z=0.291.